



LAWRENCE
LIVERMORE
NATIONAL
LABORATORY

The Parametric Sensitivity of CAM5's MJO

J. S. Boyle, S. A. Klein, D. D. Lucas, H. Y. Ma, J.
Tannahill, S. Xie

August 29, 2014

Journal of Geophysical Research - Atmosphere

Disclaimer

This document was prepared as an account of work sponsored by an agency of the United States government. Neither the United States government nor Lawrence Livermore National Security, LLC, nor any of their employees makes any warranty, expressed or implied, or assumes any legal liability or responsibility for the accuracy, completeness, or usefulness of any information, apparatus, product, or process disclosed, or represents that its use would not infringe privately owned rights. Reference herein to any specific commercial product, process, or service by trade name, trademark, manufacturer, or otherwise does not necessarily constitute or imply its endorsement, recommendation, or favoring by the United States government or Lawrence Livermore National Security, LLC. The views and opinions of authors expressed herein do not necessarily state or reflect those of the United States government or Lawrence Livermore National Security, LLC, and shall not be used for advertising or product endorsement purposes.

The Parametric Sensitivity of CAM5's MJO

J. S. Boyle^{1,2}, S. A. Klein¹, D. D. Lucas¹, H.-Y. Ma¹, J. Tannahill^{1,2}, and
S. Xie¹

¹*Program for Climate Model Diagnosis and Intercomparison, Lawrence
Livermore National Laboratory, Livermore, California, USA*

²*Retired*

Submitted to *Journal of Geophysical Research – Atmospheres*, August 2014

Corresponding author: S. A. Klein, Program for Climate Model Diagnosis and
Intercomparison, Lawrence Livermore National Laboratory, 7000 East Avenue, L-103,
Livermore, CA 94551. (klein21@llnl.gov)

Running Title: Parametric Sensitivity of CAM5's MJO

Key Points

- Parameter values that improve CAM5's Madden-Julian Oscillation are identified
- Both microphysical and macrophysical deep convection parameters are important
- Simultaneously simulating the MJO and mean climate is challenging

Abstract

We systematically explore the ability of the Community Atmospheric Model Version 5 (CAM5) to simulate the Madden-Julian Oscillation (MJO), through an analysis of MJO metrics calculated from an 1100-member perturbed parameter ensemble of 5-year simulations with observed sea-surface temperatures. Parameters from the deep convection scheme make the greatest contribution to variance in MJO simulation quality with a much smaller contribution from parameters in the large-scale cloud, shallow convection and boundary layer turbulence schemes. Improved MJO variability results from a larger lateral entrainment rate and a shorter convective adjustment timescale. Improved variability also results from reductions to the drying tendencies of deep convection that were achieved by a smaller auto-conversion of cloud to rain water and a larger evaporation of convective precipitation. Unfortunately, simulations with an improved MJO also have a significant negative impact on the climatological values of low-level cloud and absorbed shortwave radiation, suggesting that structural in addition to parametric modifications to CAM5's parameterization suite are needed in order to simultaneously well simulate the MJO and mean-state climate.

1. Introduction

Since its discovery and initial description by *Madden and Julian* [1971], the Madden-Julian Oscillation (MJO) has been shown to be a dominant mode of Tropical intra-seasonal variability with worldwide impacts [*Zhang*, 2005; *Lau and Waliser*, 2012]. The MJO is characterized by an eastward-propagating, equatorially-trapped baroclinic oscillation in the tropical wind field and is associated with precipitation anomalies that propagate from the western Indian Ocean to the western Pacific ocean with a characteristic oscillation period of 40-50 days. Unlike other types of large-scale equatorial wave modes, the existence of the MJO is not predicted by simple shallow water theory [*Wheeler and Kiladis*, 1999]. Perhaps as a result, there has not yet been established a comprehensive theory for the interactions of convective systems and large-scale dynamics that create the MJO. Consequently, improved MJO understanding relies on empirical studies utilizing satellite and field-campaign observations and models ranging from general circulation models (GCMs) to cloud resolving models [*Zhang et al.*, 2013].

Despite the lack of a comprehensive theory, there is a significant understanding of the necessary ingredients for the MJO. Most prominent are the role of moisture anomalies and the sensitivity of convection to tropospheric moisture [*Bladé and Hartmann*, 1993; *Sperber*, 2003; *Benedict and Randall*, 2007; *Maloney*, 2009; *Del Genio*, 2011; *Del Genio et al.*, 2012; *Randall*, 2013; *Sobel and Maloney*, 2013]. During the suppressed phase of the MJO (to the east of the convective center), convection depth is limited by a dry free troposphere, but shallow cumuli moisten the atmosphere at the level at which they detrain. This moistening potentially allows later convective events to rise through a more

humid atmosphere and thus penetrate somewhat higher, further recharging tropospheric moisture, until the column is sufficiently humid to trigger the deep convection that characterizes the disturbed MJO phase. The deep convection organizes and discharges the built-up moisture through precipitation and compensating subsidence drying, returning the atmosphere to the suppressed MJO phase. A complementary understanding involves the variations of the diabatic heating with MJO phase [Lin *et al.*, 2004; Zhang and Mu, 2005; Fu and Wang, 2009; Seo and Wang, 2010; Zhang *et al.*, 2010; Khouider *et al.*, 2011; Lappen and Schumacher, 2012]. Previous authors have variously emphasized the role of low-level heating in the build-up phase or the high-level heating associated with stratiform precipitation during the active phase of convection, or its combined effect of a east-to-west tilt in the level of maximum diabatic heating.

Of key interest in this study is the representation of the MJO in GCMs. While an unconventional GCM in which the conventional convective parameterization has been replaced by a two dimensional cloud resolving model can convincingly simulate the space-time structure of the MJO [Thayer-Calder and Randall, 2009; Stan *et al.*, 2010], the typical conventional GCM simulates an MJO that is too weak, if present at all [Slingo *et al.*, 1996; Lin *et al.*, 2006; Kim *et al.*, 2009; Jiang *et al.*, 2014]. However, even with conventional GCMs, there have been some encouraging results in individual models. In particular, improved simulation results from inhibiting the deep convection either with more restrictive closure assumptions [Sperber *et al.*, 2005; Zhang and Mu, 2005; Lin *et al.*, 2008; Benedict *et al.*, 2013] or by increasing the lateral entrainment in convective updrafts which enhances the sensitivity of the convection scheme to free tropospheric moisture [Tokioaka *et al.*, 1988; Bechtold *et al.*, 2008; Del Genio *et al.*, 2012; Kim *et al.*,

2011; Zhou *et al.*, 2012; Hirons *et al.*, 2012]. Given moisture's central role, it is not surprising that some improvements can also be found by altering the moistening tendencies of convection, for example by increasing the amount of evaporation of convective rain [Maloney, 2009; Del Genio *et al.*, 2012]. While model resolution does not consistently impact a simulated MJO [Crueger *et al.*, 2012; Holloway *et al.*, 2013], an interactive ocean usually improves the MJO simulation [Waliser *et al.*, 1999; Sperber *et al.*, 2005; Woolnough *et al.*, 2007; Jiang *et al.*, 2014]. However, the lack of an interactive ocean is not viewed as the primary cause of poor simulations in atmosphere-only models, as many coupled ocean-atmosphere models have a poor MJO [Lin *et al.*, 2006].

In this study, we examine the parametric sensitivity of the MJO simulation by the Community Atmosphere Model Version 5 (CAM5) [Neale *et al.*, 2011]. While this version of the model includes an entraining plume in its deep convection scheme [Neale *et al.*, 2008] that improved the MJO in Version 4 of the coupled-ocean atmosphere model [Subramanian *et al.*, 2011, Zhou *et al.*, 2012], the MJO is poorly simulated in atmosphere-only versions of CAM4 [Lappen and Schumacher, 2012] and CAM5 [see figures below and Jiang *et al.*, 2014]. Given the poor simulation of the MJO by CAM5 and the history of sometimes successful tinkering with the CAM parameterizations, the question arises: Are there any choices of parameterization settings that could enable a good simulation of the MJO? If so, would the improved simulation be consistent with current understanding of the physical processes underlying the MJO?

To that end, we examine the MJO characteristics in a large ensemble of perturbed parameter simulations of CAM5. Because the ensemble perturbs 22 uncertain parameters across all major moist physical parameterizations, it gives one the opportunity to more

fully explore the multi-dimensional parameter space, thus addressing the problem that most model developers perform sensitivity tests in an ad-hoc one-at-a-time manner. In the case of CAM5, perturbed parameter ensembles have been previously used to study the sensitivity of several precipitation characteristics including the mean and convective/stratiform ratio [Yang *et al.*, 2013] as well as the diurnal cycle and precipitation intensity distribution [Qian *et al.*, 2014]. These studies demonstrate that in some cases, altering parameter values can improve model simulations in a significant way; whether or not this is true for the simulated MJO is the focus of this paper.

The structure of the paper is as follows: Section 2 describes the model, perturbed-parameter-ensemble, and observations used. Section 3 describes the metrics that quantify MJO simulation quality, applies them to the ensemble, and presents an analysis of their parametric sensitivity. In Section 4, another model simulation is described and additional model diagnostics performed to test whether the suggestions from the sensitivity analysis actually do improve the simulated MJO. Also presented in this section is a description of changes to the mean-state climate that result from this attempt to improve the MJO. The paper ends in Section 5 with a discussion of the major conclusions.

2. The model, ensemble, and observations used

2.1. CAM5

The GCM used here is the Community Atmosphere Model Version 5 (CAM5) [Neale *et al.*, 2011], specifically version cam5_1_02. All simulations use the finite volume dynamical core with a horizontal resolution of $1.9^\circ \times 2.5^\circ$ latitude by longitude and 30 vertical levels. Table 1 contains the descriptions of the parameterizations used in

CAM5. Of note is that the deep convection parameterization is based upon Zhang-McFarlane [Zhang and McFarlane, 1995], but modified to include an entraining plume and cumulus momentum transport [Neale *et al.*, 2008].

2.2. Perturbed parameter ensemble

The CAM5 perturbed-parameter ensemble used here was performed for another project and is fully described elsewhere (see specifically the C-Ensemble in Qian *et al.* [2014]). In brief, all members of the ensemble were CAM5 integrations of 5 years length using monthly mean observed sea-surface temperatures from 2000 to 2004. The ensemble consists of 1100 members (actually five separate ensembles of 220 simulations each) that were generated with Latin Hyper-Cube sampling for the values of 22 parameters that span CAM5's convection (shallow and deep), cloud, and turbulence parameterizations. All parameters are varied simultaneously with each parameter having a uniform distribution of values over all ensemble members. Table 2 shows the default value and ranges of the parameters varied. Parameter uncertainty ranges were determined by expert solicitation based upon physical considerations. Selected parameters of the deep convection scheme are described in more detail in Appendix A; the rest of the parameters have extended descriptions in the CAM5 scientific description [Neale *et al.* 2011].

2.3. Observations and analysis data

The following precipitation datasets are used to characterize the observed MJO: the Global Precipitation Climatology Project (GPCP) [Adler *et al.*, 2003], the Tropical Rainfall Measuring Mission (TRMM) [Huffman *et al.*, 2007], and (as a precipitation surrogate) outgoing longwave radiation (OLR) estimates from Liebmann and Smith

[1996]. Daily estimates for these products are available for the years 1996 to 2009 for GPCP, 2000 to 2009 for TRMM, and 1980 to 2011 for the OLR estimate. For large-scale winds associated with the MJO, we use re-analysis data for the years 1980 to 2011 from the European Centre for Medium-Range Weather Forecasts (ERA-Interim) [Dee *et al.* 2011].

For characterization of model climate, we additionally use satellite estimates of radiation from the Clouds and Earth's Radiation Energy Systems (CERES) Energy Balanced And Filled (EBAF) dataset [Loeb *et al.*, 2009] and oceanic cloud liquid water path from the National Aeronautics and Space Administration Water Vapor Project (NVAP) [Randel *et al.*, 1996].

3. An analysis of the MJO sensitivity in the ensemble

3.1. Metrics for the MJO and their variability in the ensemble

The comprehensive diagnostics described in *CLIVAR* [2009] were reviewed to determine appropriate measures to characterize the MJO in the perturbed parameter ensemble, subject to the constraint that precipitation was the only sub-monthly output available. Three diagnostics that appear to be powerful at discriminating the MJO were selected and for each the information was further reduced into a single number or 'metric'. The analysis was restricted to the boreal winter months of November to April, the months with the most pronounced MJO activity.

The first two metrics can best be described by reference to Figure 1, which shows time lag – longitude plots of correlation coefficients between 10°S - 10°N averaged intra-seasonal TRMM precipitation anomalies with intra-seasonal precipitation for a base

region in the Indian Ocean region (Figure 1a, 70°E -90°E, 5°S - 5°N) and the Western Pacific Ocean (Figure 1b, 130°E - 150°E, 5°S to 5°N). Intra-seasonal precipitation was calculated with a band-pass filter of 20 to 90 days. These plots show the progression of MJO precipitation eastward from the Indian Ocean into the West Pacific Ocean. Corresponding figures were constructed for each ensemble member and the first metric (called *patCorACIO*) was set equal to the pattern correlation coefficient over the plotted domain (30°E - 180°E, -20 - +20 days) between the model result and the observed using the Indian Ocean base region (Figure 1a). The second metric (called *patCorACWP*) was created in an identical fashion but with using the Western Pacific Ocean base region. For both metrics, a perfect model result would be indicated by a metric with value of +1.0 (perfect correlation).

The third metric is described by reference to Figure 2 which displays the November to April wavenumber frequency spectra of 10°S - 10°N averaged TRMM precipitation. The computation was carried out as described by *CLIVAR* [2009]. The actual metric (called *wePwrRatio*) is the ratio of power in Eastward to Westward propagating waves. The power is calculated for frequencies with periods between 20 and 90 days and zonal wavenumbers 1 to 5. In Figure 2, this ratio is computed from the average power over the two outlined boxes. For TRMM, *wePwrRatio* has a value of 2.18.

These metrics are complementary since *patCorACIO* and *patCorACWP* capture the MJO phase speed and geographical characteristics whereas *wePwrRatio* provides a measure of MJO magnitude and scale.

Figure 3 displays the joint histogram of *patCorACIO* and *wePwrRatio* calculated from all 1100 members of the ensemble as well as from a separate integration of CAM5

when run with the default parameter settings. Figure 3a displays the results of metrics calculated using the GPCP precipitation estimate and Figure 3b presents the results using TRMM precipitation. Although the exact values of *wePwrRatio* and *patCorACIO* do vary with the choice of precipitation datasets, the general impression remains the same. Namely, the default model and the majority of models in the ensemble do not perform particularly well using these metrics, with a relatively low pattern correlation (typically less than 0.5) and no preference for eastward propagating low-frequency waves unlike the observations. Despite this, there are a few dozen or so ensemble members that do perform relatively well with pattern correlations in excess of 0.7 and East-West power ratios approaching 2. Results using *patCorACWP* instead *patCorACIO* are similar.

3.2. The parametric sensitivity of the MJO metrics and a Bayesian parameter estimation

Given the wide range of model performance across the ensemble, it may be possible to identify which parameters influence the simulated metrics and which parameters are immaterial to the simulation of the MJO. A further goal would be to estimate the optimal value for each parameter given the observed value of the metrics. These goals are accomplished using statistical techniques described in Appendix B that specialize in the analysis of variance and parameter estimation.

Figure 4 summarizes the relative importance of the perturbed parameters in explaining variance in the simulated *patCorACIO*, *patCorACWP* and *wePwrRatio*. Larger values of feature scores, roughly analogous to the fraction of variance explained, indicate greater impact of a parameter. For all metrics, parameters from the deep convection scheme dominate the ensemble variance with perhaps surprising little

influence from parameters from other parameterization schemes. The most important parameters are the timescale for deep convection (*zmconv_tau*) and the mass entrainment rate (*zmconv_dmpdz*), with the parameters controlling precipitation and evaporation efficiency (*zmconv_c0_ocn* and *zmconv_ke*, respectively) and the magnitude of the downdraft mass-flux (*zmconv_alfa*) also being important, particularly for *patCorACIO* and *patCorACWP*.

Recommended values for these parameters can be discerned from Figure 5 which shows the marginal parameter posterior distributions for *zmconv_tau*, *zmconv_dmpdz*, *zmconv_c0_ocn*, *zmconv_ke* and *zmconv_alfa* over their normalized range from 0 (minimum value) to 1 (maximum value). The red vertical lines indicate the normalized values that correspond to CAM5's default parameter settings. Larger values indicate increased likelihood of that parameter value leading to a simulation that would improve the agreement of with the observed values of *patCorACIO*, *patCorACWP* and *wePwrRatio*. The figure suggests than an improved simulation would result from setting *zmconv_c0_ocn*, *zmconv_tau* and *zmconv_alfa* to their minimum values and *zmconv_dmpdz* and *zmconv_ke* to their maximum values. Because the most likely parameter values fall at the boundaries of the parameter sampling ranges, it suggests that true optimum values of these parameters may lie outside the sampled ranges of the parameters. Because the parameter ranges are set by expert judgment regarding their physical plausibility, an optimal value outside the specified ranges may indicate structural deficiencies in the physical parameterizations of the climate model [Neelin *et al.*, 2010].

4. Can the MJO be improved, and if so, what are the consequences for the mean climate?

4.1. The MJO of a targeted simulation

The sensitivity analysis presented in the previous section provides guidance as to which parameters the simulated MJO metrics are sensitive to and recommends suggested values. However, because no single run in the ensemble changed all of the parameters in the recommend way and all runs contain changes to other parameters that were at best insignificant to the MJO, it remains to be demonstrated that this guidance would actually improve the simulated MJO. Furthermore, model optimization of these three metrics may not produce a realistic MJO when one considers MJO characteristics other than those measured by the metrics.

Thus, a targeted new simulation (called *UQ-Rec*) was performed in which the only parameters changed were those in the deep convection parameterization suggested by the sensitivity analysis to have an influence on the simulated MJO (see Appendix A for their description). Specifically, the rate at which liquid is converted into rain inside the updraft over ocean (*zmconv_c0_ocn*) is set to the lower limit from Table 2, a reduction by a factor of 45 with respect to the default. Second, the evaporation of convective precipitation was increased by raising the efficiency parameter (*zmconv_ke*) by a factor of 10, setting its value equal to the upper limit from Table 2. Both changes reduce the drying tendencies of deep convection, effectively lowering its precipitation efficiency. Third, the convective time scale (*zmconv_tau*) was set to its lower limit from Table 2, effectively doubling the cumulus mass-flux for a given large-scale condition. No

changes were made to the other two parameters (*zmconv_dmpdz* and *zmconv_alfa*), since Figure 5 suggests that little additional gain would result, given that the likelihood of the default setting is nearly as large as the maximum likelihood in the tested range.

In order to increase the statistical robustness, a ten-year simulation for *UQ-Rec* covering the years 2000-2009 was performed. As a point of comparison, two additional ten-year simulations were also performed for the model with the default parameter settings (called *Default*) and the single member of the perturbed parameter ensemble that scored best in terms of the MJO metrics (called *PPE-Best*). While all 22 parameters in *PPE-Best* differ in their settings from their defaults, *PPE-Best* shares similarities to *UQ-Rec* including a factor of 15 reduction in *zmconv_c0_ocn* relative to the default CAM5, a halving of *zmconv_tau*, and a factor of 2.5 increase in *zmconv_ke*.

The analysis of the simulated MJO in these runs begins with an examination of the diagnostics upon which the MJO metrics are based. Figure 6 shows the lag-longitude plots of boreal winter intra-seasonal precipitation anomalies (color shading) for the TRMM observations and the three model runs correlated with Indian ocean intra-seasonal precipitation. Overlain on these plots are the correlation coefficients for the 850 hPa zonal wind anomalies with Indian ocean intra-seasonal precipitation. The *UQ-Rec* appears to have better eastward propagation for both the OLR and 850 hPa wind anomalies, especially over the Indian Ocean and west Pacific. In the other two simulations, the OLR tends to show more of a standing oscillation over the Indian Ocean, with pronounced westward propagation of 850 hPa wind anomalies.

The improved eastward propagation in the *UQ-Rec* simulation is also confirmed in Figure 7, which displays the wavenumber – frequency spectra of tropical precipitation

from the model simulations calculated in the same way as that of the observations shown in Figure 2. Here there are striking differences in magnitude of intra-seasonal variance (consider the different color scales) with the *PPE-Best* and particularly *UQ-Rec* simulations having considerably larger amounts of intra-seasonal variance relative to that in the *Default* simulation. The increased variances are accompanied by significant increases in the ratio of Eastward to Westward propagating waves with the value of the *wePwrRatio* in the *UQ-Rec* simulation (2.01) lying within the range of the observed estimates. However, accompanying these improvements are some persistent deficiencies including a tendency for the maximum power to occur at too low a frequency (in both eastward and westward propagating variance) and for variance to peak at wave number two without extending to wave number one as in observations. These behaviors have also been found in other models [Kim *et al.* 2009].

Extending the analysis to other MJO diagnostics (often following *CLIVAR* [2009]), Figure 8 shows the first multivariate combined Empirical Orthogonal Function (CEOF) of the 20 – 90 day band-passed OLR, 850 and 200 hPa zonal winds averaged from 15°S to 15°N for the boreal cool season for the observations and models calculated as in *Wheeler and Hendon* [2004]. While all simulations exhibit the out-of-phase relationship between 850 hPa and 200 hPa zonal winds as seen in the observations, they all struggle to exhibit the observed quadrature relationship for OLR with winds in the Indian ocean. In terms of the fraction of variance explained, the *UQ-Rec* simulation has the highest fraction of variance explained (18.8%) which while still less than observed (22.9%) is noticeably higher than that of the *Default* (14.9%). Results are similar for the second CEOF (not shown), which explains a similar amount of variance as CEOF 1 (in

both the models and observations). Here too, the relative superiority of the *UQ-Rec* simulation is illustrated by the values of the correlation coefficient and lag time with the maximum correlation between the principal component (PC) time-series corresponding to CEOF 1 and CEOF 2. In particular, the values from the *UQ-Rec* simulation (0.76 and 9 days) are closer to the observed values (0.78 and 10 days) than are the values from the *Default* simulation (0.61 and 9 days). This indicates an improved temporal coherency for the eastward propagating signal.

MJO amplitude can also be gauged from Figure 9, which shows power-spectral density plots of the CEOF 1 (Figure 8) projected onto the unfiltered data (with only the seasonal cycle removed). Of all the simulations, the *UQ-Rec* has by far the largest amplitude across all frequencies although it must be noted its amplitude is still less than observed. Furthermore, all simulations have too much amplitude in the lowest frequency near 100 days with the frequency of the peak power shifted by 20 - 30 days from the observations.

For a qualitative overview of the structure of the MJO simulations, Figure 10 is a composite of November to April band-passed OLR as a function of MJO phase for the observations and the three simulations. The composites are based on $PC1^2 + PC2^2 > 1$ in each octant of the PC1 vs. PC2 phase space, where PC1 and PC2 are the unit standard deviation principal components corresponding to CEOF 1 and CEOF 2. The *Default* simulation has an almost no evidence of a definitive MJO structure. In contrast, the *UQ-Rec* simulation has a fairly good correspondence with observations with its weakest point being in phase 5 when it substantially underestimates the signal over the Maritime Continent. Curiously, the *PPE-Best* simulation has poor features at the initial and final

phases but does rather well at phase 5. The improved result over the land of the maritime continent in the *PPE-Best* simulation may be because *zmconv_c0_land* is a factor of 4 less than in the *Default* and *UQ-Rec* simulations.

Figure 11 is a similar composite but for the 850 hPa zonal wind. While the general character of the *Default* simulation appears reasonable, its amplitude is smaller than the observations. In contrast, the amplitudes of the fluctuations are larger (and perhaps a bit too large relative to observations) for the *PPE-Best* and *UQ-Rec* simulations. The generally better performance of the simulations for the 850 hPa zonal wind relative to OLR is symptomatic of the fact that the large-scale dynamics is easier to simulate relative to that of the precipitation [Crueger *et al.*, 2012].

From the literature cited in the introduction, one would expect that the eastward moving convection center would be preceded by low-level moistening and heating with upper level moistening and mid to lower level clearing in its wake. Figure 12 presents longitude-pressure cross-sections of specific humidity anomalies from 15°S to 15°N linearly regressed onto the 20 – 90 day band-passed precipitation at 120°E. The re-analysis shows significant low-level positive anomalies to the east of 120°E with mid-level drying to the west. The *UQ-Rec* simulation has a pattern in many respects similar to the re-analysis including positive moisture anomalies beneath 900 hPa to the east of 120°E, and negative moisture anomalies to the west. The other model simulations fail to show the positive low-level moisture anomalies to the east.

Figure 13 is the same as Figure 12 except for displaying the anomalies in moist diabatic heating (convective plus stratiform). The estimate from the ERA-Interim for this can be found in Figure 10a of Benedict *et al.* [2013]. Of the three model simulations, the

UQ-Rec simulation has the most pronounced low-level heating to the east of 120°E and is most close to the re-analysis.

4.2 What are the consequences for the mean model climate state?

Figures 6 to 13 indicate that modifying a few parameters of the deep convection scheme as done in the *UQ-Rec* model configuration improves the simulated MJO. However, these parameter settings may not be acceptable for the model if the simulation of the mean climate were seriously degraded. In terms of mean precipitation, the *UQ-Rec* simulation performs nearly as well as the *Default* with a 40% smaller bias and 2.5% increase in root-mean-square error (Table 3). Relative to the *Default*, the *UQ-Rec* simulation has increased precipitation on the equator in the Western Pacific and in the South Pacific Convergence Zone with reduced precipitation in the Northern Hemisphere Tropics which is an improvement (not shown). In the *UQ-Rec* simulation, the fraction of precipitation produced from the stratiform or large-scale cloud parameterization increases to 11% from 6% in the *Default* simulation. This is less than the 30% stratiform precipitation fraction that was thought to be important for the MJO simulation of two other models [Fu and Wang, 2009; Seo and Wang, 2010].

However, in terms of the climatological radiation field, a very strong bias in excess of 20 W m⁻² has been introduced into the global mean shortwave radiation cloud radiative effect through the modification of perturbed parameters in both the *UQ-Rec* and *PPE-Best* simulations (Table 3). A bias of this magnitude is unacceptable for a climate model. This increase in reflected shortwave radiation is due to a very large increase in column integrated liquid water path (LWP), with values in the *UQ-Rec* and *PPE-Best* simulations that are 4 times that observed. A single perturbation experiment (called

OAT38) changing only *zmconv_c0_ocn* suggests that the decrease in this parameter is responsible for most of this increase in LWP and reflected shortwave radiation. Physically, by lowering the rate at which convective cloud condensate is converted to precipitation, more convective condensate is left as cloud water that can reflect shortwave radiation. A related consequence is an increase in lower tropospheric moisture (Figure 14). Compared to the *Default* simulation and the re-analysis, all modified simulations exhibit a considerably moister lower troposphere with typical increases of 2 g kg^{-1} particularly in the layer between 500 and 800 hPa. These are the same levels that contribute to the very strong increase in LWP.

It is clear if one were to use the guidance from this study to improve CAM5's MJO, one would need to eliminate these biases in clouds and reflected shortwave radiation. Given that a bias of this magnitude is likely outside of the range that could be eliminated with further parameter modifications (i.e. routine model tuning), structural modifications to CAM5's parameterization suite would be needed.

5. Discussion

The motivating question for this study was: *Are there any choices of CAM5's parameterization settings that could enable a good simulation of the MJO?* The answer seems to be a qualified yes. By modifying 5 key parameters in the deep convection parameterization based upon guidance from a very large perturbed-parameter ensemble, the simulation of the MJO is improved, particularly in terms of the amplitude of the intra-seasonal variability and the simulation of low-level moisture and heating anomalies to the east of the convective center. However, the improved MJO still has noticeable deficiencies, particularly with an oscillation period that is too long. This would seem to

be a qualified success for the perturbed-parameter methodology; namely, metrics for the MJO were defined *a priori*, a sensitivity analysis then found the parameters that influence the metrics, and *a posteori* simulation demonstrated that guidance from the sensitivity analysis was correct. Note that partial success was not guaranteed from the start; two other possibilities were that no perturbations to the parameters chosen would have successfully improved the MJO, or that the analysis techniques could have missed possible ways to improve the MJO. However, given the systematic nature of the UQ exploration, we are confident that we have found the only ways to improve the MJO in CAM5 based on modification to the 22 parameters considered.

The major drawback of this approach is that fixing one aspect of the simulation may introduce problems into other aspects of the model's simulation. While the simulation of climatological precipitation is acceptable, the mean amount of absorbed shortwave radiation is unacceptably reduced, primarily as a result of the one parameter (*zmconv_c0_ocn*) that is most effective at improving the MJO. It should also be noted that the tunings suggested here are in apparent disagreement with those suggested from other perturbed-parameter studies with CAM5 to improve other aspects of the simulated precipitation field. In particular, to improve the ratio of stratiform to convective scale precipitation, *Yang et al.* [2013] suggest that lengthening the convective adjustment time scale (*zmconv_tau*) and increasing the initial downdraft mass-flux (*zmconv_alfa*) relative to CAM5's default settings; guidance which is opposite to that found here for improving the MJO. *Qian et al.* [2014] also suggest that the adjustment time scale (*zmconv_tau*) should be lengthened to increase the value of the 95th percentile of hourly mean precipitation distribution.

426 In terms of the physics of convection and its relationship to the MJO, the present
 427 study confirms the now well-known sensitivity of tropical variability to the lateral
 428 entrainment rate of the deep convection scheme. The present study also confirms the
 429 previously known importance of processes that affect the ultimate drying tendencies of
 430 the deep convection parameterization, including both the rate at which convective
 431 precipitation evaporates and the representation of cloud microphysics in the
 432 parameterized convective updrafts. But there are differences too with prior work. In
 433 particular, the simulation of the MJO is improved by shortening the adjustment time scale
 434 for deep convection for which we do not have a physical explanation. Also somewhat
 435 surprising is the relative insensitivity to parameters from processes other than the deep
 436 convection scheme. If the buildup of moisture in advance of the MJO deep convective
 437 phase is so important, why weren't the simulations of the MJO sensitive to the mixing
 438 (*uwshcu_rkm* and *uwshcu_rpen*) or microphysical (*uwshcu_criqc* and *uwshcu_kevp*)
 439 parameters in the shallow convection scheme [Cai *et al.*, 2014]? Likewise, if the radiative
 440 heating associated with clouds is an important amplifier on the variability of tropical
 441 convection, why weren't the simulations of the MJO sensitive to changes in the key ice
 442 microphysical parameters (*cldwatmi_dcs*, *cldwatmi_ai*, and *cldwatmi_as*) that affect the
 443 amount of ice in high-level stratiform anvils associated with convection? Two possible
 444 answers to these questions are (a) that these parameters were not perturbed over a wide
 445 enough range to simulate a noticeable effect or (b) it may be that shallow convection and
 446 radiative heating (at least in CAM5, if not nature) are not that important to the MJO. A
 447 further caution on the guidance from perturbed parameter ensembles is that the

recommend parameter values may improve the simulation of the phenomenon for the wrong physical reason [*Hannah and Maloney, 2014*].

Clearly discretion should be exercised as to how and when it is suitable to use parameter perturbations to improve the simulation of selected phenomena. Perhaps the knowledge gained in this paper might be useable in a qualitative way in future tuning exercises with CAM when other significant model changes in either in resolution or model physics have occurred. For example, knowledge of which parameters affect the simulated MJO can be used when making choices in an ultimate tuning of a climate model, when it is necessary to balance the simulation quality of a model across many diverse metrics. The other way in which the knowledge gained in this study may be useful is in the encouragement of the development of separate structural changes to model physics. In light of the results presented here, parameterization developments for the CAM aimed at increasing the sensitivity of the deep convection scheme through treatments of mesoscale organization [*Mapes and Neale, 2011; Park, 2014*] and reducing the drying tendencies of deep convection parameterizations through alterations to the treatment of convective-scale microphysics [*Song et al., 2012*] would seem promising as means to improve the MJO.

466 **Acknowledgments**

467 Work at LLNL was performed under the auspices of the U. S. Department of Energy
468 (DOE) by Lawrence Livermore National Laboratory under contract No. DE-AC52-
469 07NA27344. The efforts of the authors were funded by the Regional and Global Climate
470 Modeling and Earth System Modeling programs and the Scientific Discovery through
471 Advanced Computing project of the U. S. Department of Energy's Office of Science. The
472 perturbed parameter ensemble analyzed in this study was performed for the Climate
473 Science for Sustainable Energy Future project supported by the Earth System Modeling
474 program. Given the very large quantities of data involved, only summaries of simulation
475 output can be made available upon request from the authors. The authors appreciate
476 conversations with Richard Neale, Brian Mapes, and Leo Donner. Comments on the
477 manuscript provided by Ken Sperber are appreciated.

Appendix A: Description of selected parameters in CAM5's Zhang-McFarlane cumulus parameterization

The production rate of rain water (R_r) from cloud liquid water in the Zhang-McFarlane cumulus parameterization is given by:

$$R_r = C_0 M_u Q_l \quad (\text{A1})$$

where M_u is the updraft mass flux, C_0 is the autoconversion coefficient, and Q_l is the cloud liquid water content. Smaller values of C_0 decrease the rate of conversion of cloud water to rain. In CAM5, C_0 is permitted to have different values over land and ocean and corresponds to the entries *zmconv_c0_lnd* and *zmconv_c0_ocn* in Table 2.

The closure condition assumes that cumulus convection consumes Convective Available Potential Energy (*CAPE*) at a certain rate F per unit updraft mass flux at cloud base (M_b). Knowing F , M_b is calculated as:

$$M_b = \frac{CAPE - CAPE_0}{\tau F} \quad (\text{A2})$$

where $CAPE_0$ is the threshold for deep convection and τ is a prescribed time scale during which *CAPE* in excess of $CAPE_0$ is consumed by convection. τ corresponds to the entry *zmconv_tau* in Table 2.

The rate of evaporation of precipitation E_k directly into the grid scale environment as it falls to the surface is given by:

$$E_k = K_e (1 - RH_k) R_k^{1/2} \quad (\text{A3})$$

497 where R_k is the total rainwater flux in model layer k , RH is the relative humidity of the
 498 environment, and K_e is the evaporation efficiency. K_e corresponds to the entry
 499 *zmconv_ke* in Table 2.

500 In the original Zhang-McFarlane scheme, $CAPE$ is diagnosed by assuming an
 501 undiluted parcel ascent. However, in CAM5, deep convection is assumed to take place
 502 with an entraining air parcel that mixes with the free troposphere proportional to an
 503 assumed constant entrainment rate [Neale *et al.*, 2008; Zhou *et al.* 2012]. The entrainment
 504 rate corresponds to the entry *zmconv_dmpdz* in Table 2.

505 Downdrafts are assumed to start at the mid-tropospheric minimum in saturated
 506 moist static energy and detrain in the sub-cloud layer. The downdraft mass flux is scaled
 507 with the updraft mass-flux where the proportionality factor α is given by:

$$508 \quad \alpha = \frac{\mu P}{P + E_d} \quad (A2)$$

509 where P is the total precipitation in the convective layer and E_d is the rain water
 510 evaporation required to maintain the downdraft in a saturated state. This formalism
 511 ensures that the downdraft mass flux vanishes in the absence of precipitation, and that
 512 evaporation cannot exceed some fraction μ of the precipitation. μ corresponds to the entry
 513 *zmconv_alfa* in Table 2.

514

Appendix B: Sensitivity analysis and Bayesian parameter estimation

Two stages of analysis were performed on the *patCorACIO*, *patCorACWP* and *wePwrRatio* metrics calculated from the perturbed-parameter ensemble. First, a parameter sensitivity analysis was performed to identify the perturbed parameters (also called input parameters here) that are most responsible for the variance in the MJO metrics. Second, given observational targets for *patCorACIO*, *patCorACWP* and *wePwrRatio*, a Bayesian parameter estimation was applied to determine posterior distributions for those parameters identified in the first stage to be most responsible for the variance in the metrics. Both stages utilized statistical response surface models that relate the values of the CAM5 parameters to the MJO metrics. Before fitting these response surface models, the *patCorACIO*, *patCorACWP* and *wePwrRatio* distributions were centered to have a mean of 0 and unit standard deviation. For the parameter sensitivity analysis, 80% of the data was randomly selected for fitting the response surface models and the remaining 20% used for testing quality of the fits.

In the first stage, the sensitivity analysis was conducted using response surface models for *patCorACIO*, *patCorACWP* and *wePwrRatio* as a function of the 22 input parameters. Although other methods including linear basis functions, polynomial chaos expansions [Lucas *et al.*, 2013], and support vector machines [Bishop, 2007] were tried, random forests [Breiman, 2001] were selected as they yielded the best fits. Briefly, a random forest is an ensemble of randomized decision trees. Individual trees in the forest are generated by bootstrap sampling with replacement of the training data and selecting random subsets of the input parameters for partitioning the input data space. A variant of

random forests, called extremely randomized trees [Geurts *et al.*, 2006], was used that adds a further level of randomization to the partitioning. Random forests are straightforward to fit and attractive because they make essentially no assumptions about the relationships in the data. The extra trees implementation contained in the Scikit-learn package [Pedregosa *et al.*, 2011] was used with all of its default settings except the number of trees, which was set to 50. From the random forests, parameter sensitivities with error estimates were derived in terms of feature scores that approximate the fraction of ensemble variance explained by the parameter variations. Important parameters have large feature scores and the error estimates are traceable to the variability in the ranks across trees in the forest.

In the second stage, Bayesian parameter estimation was performed for the five parameters with the largest feature scores. The goal is to determine the parameter values that hypothetically would improve the agreement between the simulated and observed values of *patCorACIO*, *patCorACWP* and *wePwrRatio*. Response surfaces are an indispensable tool for this analysis because they are used to quickly estimate the values of the metrics at new, untested values of the input parameters without the need to run additional CAM5 simulations. To that end, the random forest response surfaces were refit using only the selected parameters from all ensemble members. Subsequently, Bayes' rule ($\text{posterior} \propto \text{likelihood} \times \text{prior}$) is applied with samples drawn from a prescribed prior probability distribution over the parameters, and for each sample point the likelihood of explaining the observations is calculated. The likelihood and prior distributions are multiplied and normalized to yield a posterior probability distribution over the parameters. Following the parameter sampling distribution, we use uniform prior

561 distribution over the ranges of the selected parameter ranges defined in Table 2, which
 562 simplifies the Bayesian calculations (i.e. the likelihood is multiplied by 1). We draw 10^6
 563 samples from this prior distribution using Latin Hypercube Sampling, and then evaluate
 564 *patCorACIO*, the *patCorACWP* and *wePwrRatio* using the random forest response
 565 surfaces. The logarithm of the likelihood is computed as $\log L = -\left[(r_{patCorACIO} - \right.$
 566 $\left. t_{patCorACIO})^2 + (r_{patCorACWP} - t_{patCorACWP})^2 + (r_{wePwrRatio} - t_{wePwrRatio})^2\right] / 2\delta^2$,
 567 where r and t are, respectively, the centered response surface and target (i.e., observed)
 568 values of *patCorACIO*, *patCorACWP* and *wePwrRatio*, and δ^2 approximates the variance
 569 of the squared differences. The target values are taken as 1.0, 1.0 and 2.18 for
 570 *patCorACIO*, *patCorACWP* and *wePwrRatio*, and δ is set as 2.5 standard deviations of
 571 the centered distributions. Our focus is on identifying likelihood maxima (i.e. optimal
 572 parameter values) rather than determining the precise shape of the likelihood distribution
 573 (i.e. parameter uncertainties), so the actual value of the δ used is somewhat arbitrary.

References

- Adler, R. F., et al. (2003), The version-2 Global Precipitation Climatology Project (GPCP) monthly precipitation analysis (1979-present), *Journal of Hydrometeorology*, 4 (6), 1147–1167.
- Bechtold, P., M. Kohler, T. Jung, F. Doblas-Reyes, M. Leutbecher, M. J. Rodwell, F. Vitart, and G. Balsamo (2008), Advances in simulating atmospheric variability with the ECMWF model: from synoptic to decadal timescales, *Q. J. R. Meteorol. Soc.*, 137, 553–597.
- Benedict, J. J., and D. A. Randall (2007), Observed characteristics of the MJO relative to maximum rainfall, *Journal of the Atmospheric Sciences*, 64 (7), 2332–2354, doi:10.1175/JAS3968.1.
- Benedict, J. J., E. D. Maloney, A. H. Sobel, D. M. Frierson, and L. J. Donner (2013), Tropical intraseasonal variability in version 3 of the GFDL atmosphere model, *Journal of Climate*, 26(2), 426–449, doi:10.1175/JCLI-D-12-00103.1.
- Bladé, I., and D. L. Hartmann (1993), Tropical intraseasonal oscillations in a simple non-linear model, *Journal of the Atmospheric Sciences*, 50(17), 2922–2939.
- Breiman, L. (2001), Random forests, *Machine Learning*, 45(1), 5–32.
- Bretherton, C. S., and S. Park (2009), A new moist turbulence parameterization in the Community Atmosphere Model, *Journal of Climate*, 22(12), 3422–3448.
- Cai, Q., G. J. Zhang, and T. Zhou (2013), Impacts of shallow convection on MJO simulation: A moist static energy and moisture budget analysis. *Journal of Climate*, 26, 2417–2431, doi: <http://dx.doi.org/10.1175/JCLI-D-12-00127.1>

- 596 CLIVAR Madden-Julian Oscillation Working Group (2009), MJO simulation
597 diagnostics, *Journal of Climate*, 22 (11), 3006–3030.
- 598 Crueger, T., B. Stevens, and R. Brokopf (2012), The Madden–Julian oscillation in
599 ECHAM6 and the introduction of an objective MJO metric, *Journal of Climate*,
600 26(10), 3241–3257, doi:10.1175/JCLI-D-12-00413.1.
- 601 Dee, D. P., et al. (2011), The era-interim reanalysis: configuration and performance of the
602 data assimilation system, *Quarterly Journal of the Royal Meteorological Society*,
603 137 (656), 553–597, doi:10.1002/qj.828.
- 604 Del Genio, A. (2011), Representing the sensitivity of convective cloud systems to
605 tropospheric humidity in general circulation models, *Surveys in Geophysics*, pp.
606 1–20, doi:10.1007/s10712-011-9148-9.
- 607 Del Genio, A. D., Y. Chen, D. Kim, and M.-S. Yao (2012), The MJO transition from
608 shallow to deep convection in CloudSat/CALIPSO data and GISS GCM
609 simulations, *Journal of Climate*, 25(11), 3755–3770, doi:10.1175/JCLI-D-11-
610 00384.1.
- 611 Frierson, D. M. W., D. Kim, I.-S. Kang, M.-I. Lee, and J. Lin (2011), Structure of
612 AGCM- simulated convectively coupled Kelvin waves and sensitivity to
613 convective parameterization, *Journal of the Atmospheric Sciences*, 68 (1), 26–45,
614 doi:10.1175/2010JAS3356.1.
- 615 Fu, X., and B. Wang (2009), Critical roles of the stratiform rainfall in sustaining the
616 Madden- Julian oscillation: GCM experiments, *Journal of Climate*, 22(14), 3939–
617 3959.

- 618 Gettelman, A., et al. (2010), Global simulations of ice nucleation and ice supersaturation
 619 with an improved cloud scheme in the community atmosphere model, *J. Geophys.*
 620 *Res.*, *115*(D18), doi:10.1029/2009JD013797.
- 621 Geurts, P., D. Ernst., and L. Wehenkel (2006), Extremely randomized trees, *Machine*
 622 *Learning*, *63*(1), 3–42.
- 623 Hannah, W. M. and E. D. Maloney (2014), The moist static energy budget in NCAR
 624 CAM5 hindcasts during DYNAMO, *Journal of Advances in Modeling Earth*
 625 *Systems*, *06*, doi:10.1002/2013MS000272.
- 626 Hirons, L. C., P. Inness, F. Vitart, and P. Bechtold (2012), Understanding advances in the
 627 simulation of intraseasonal variability in the ECMWF model. Part I: The
 628 representation of the MJO, *Quarterly Journal of the Royal Meteorological*
 629 *Society*, doi:10.1002/qj.2060.
- 630 Holloway, C. E., S. J. Woolnough, and G. M. S. Lister (2013), The effects of explicit
 631 versus parameterized convection on the MJO in a large-domain high-resolution
 632 tropical case study. part I: Characterization of large-scale organization and
 633 propagation, *Journal of the Atmospheric Sciences*, *70*(5), 1342–1369,
 634 doi:10.1175/JAS-D-12-0227.1.
- 635 Huffman, G. J., R. F. Adler, D. T. Bolvin, G. Gu, E. J. Nelkin, K. P. Bowman, Y. Hong,
 636 E. F. Stocker, and D. B. Wolff (2007), The TRMM multisatellite precipitation
 637 analysis (tmpa): Quasi-global, multiyear, combined-sensor precipitation estimates
 638 at fine scales, *Journal of Hy-drometeorology*, *8*(1), 38–55.
- 639 Iacono, M. J., J. S. Delamere, E. J. Mlawer, M. W. Shephard, S. A. Clough, and W. D.
 640 Collins (2008), Radiative forcing by long-lived greenhouse gases: Calculations

- 641 with the AER radiative transfer models, *Journal of Geophysical Research:*
 642 *Atmospheres*, 113(D13), D13,103, doi: 10.1029/2008JD009944.
- 643 Jiang, X., et al. (2014), Exploring key processes of the Madden-Julian Oscillation (MJO):
 644 A joint WGNE MJO Task Force / GEWEX GASS project on the vertical structure
 645 and diabatic processes of the MJO – Part I. Climate simulations, *Journal of*
 646 *Geophysical Research: Atmospheres*, submitted.
- 647 Klingaman, N. P., et al. (2014), Vertical structure and diabatic processes of the Madden-
 648 Julian oscillation: Linking hindcast fidelity to simulated diabatic heating and
 649 moistening, *Journal of Geophysical Research: Atmospheres*, submitted.
- 650 Khouider, B., Y. Han, A. J. Majda, and S. N. Stechmann (2011), Multiscale waves in an
 651 MJO background and convective momentum transport feedback, *Journal of the*
 652 *Atmospheric Sciences*, 69(3), 915–933, doi:10.1175/JAS-D-11-0152.1.
- 653 Kim, D., et al. (2009), Application of MJO simulation diagnostics to climate models,
 654 *Journal of Climate*, 22(23), 6413–6436, doi:10.1175/2009JCLI3063.1.
- 655 Kim, D., A. H. Sobel, E. D. Maloney, D. M. W. Frierson, and I.-S. Kang (2011), A
 656 systematic relationship between intraseasonal variability and mean state bias in
 657 AGCM simulations, *Journal of Climate*, 24(21), 5506–5520,
 658 doi:10.1175/2011JCLI4177.1.
- 659 Lappen, C.-L., and C. Schumacher (2012), Heating in the tropical atmosphere: what level
 660 of detail is critical for accurate MJO simulations in GCMs?, *Climate Dynamics*,
 661 39 (9-10), 2547– 2568, doi:10.1007/s00382-012-1327-y.
- 662 Lau, W. K.-M., and D. E. Waliser (2012), Intraseasonal Variability in the Atmosphere-
 663 Ocean Climate System, 2nd ed., Springer, 613pp.

- 664 Liebmann, B., and C. Smith (1996), Description of a complete (interpolated) outgoing
 665 longwave radiation dataset, *Bull. Amer. Meteor. Soc.*, 77(6), 1275–1277.
- 666 Lin, J., B. Mapes, M. Zhang, and M. Newman (2004), Stratiform precipitation, vertical
 667 heating profiles, and the Madden Julian oscillation, *Journal of the Atmospheric*
 668 *Sciences*, 61(3), 296–309.
- 669 Lin, J.-L., et al. (2006), Tropical intraseasonal variability in 14 IPCC AR4 climate
 670 models. Part I: Convective signals, *Journal of Climate*, 19 (12), 2665–2690.
- 671 Lin, J.-L., M.-I. Lee, D. Kim, I.-S. Kang, and D. M. W. Frierson (2008), The impacts of
 672 convective parameterization and moisture triggering on AGCM-simulated
 673 convectively coupled equatorial waves, *Journal of Climate*, 21, 883–909.
- 674 Liu, X., and CoAuthors (2012), Toward a minimal representation of aerosols in climate
 675 models: description and evaluation in the community atmosphere model CAM5,
 676 *Geosci. Model Dev.*, 5 (3), 709–739, doi:10.5194/gmd-5-709-2012.
- 677 Lucas, D. D., and CoAuthors (2013), Failure analysis of parameter-induced simulation
 678 crashes in climate models, *Geosci. Model Dev.*, 6, 1157–1171, doi:10.5194/gmd-
 679 6-1157-2013.
- 680 Madden, R. A., and P. R. Julian (1971), Detection of a 40–50 day oscillation in the zonal
 681 wind in the tropical pacific, *Journal of the Atmospheric Sciences*, 28 (5), 702–
 682 708, doi:10.1175/1520-0469(1971)028<0702:DOADOI>2.0.CO;2.
- 683 Maloney, E. D. (2009), The moist static energy budget of a composite tropical
 684 intraseasonal oscillation in a climate model, *Journal of Climate*, 22 (3), 711–729,
 685 doi:10.1175/2008JCLI2542.1.

- 686 Mapes, B. E., and R. B. Neale (2011), Parameterizing convective organization to escape
 687 the entrainment dilemma, *J. Adv. Model. Earth Syst.*, *3*, M06004,
 688 doi:10.1029/2011MS000042.
- 689 Morrison, H., and A. Gettelman (2008), A new two-moment bulk stratiform cloud
 690 microphysics scheme in the community atmosphere model, version 3 (cam3). part
 691 I: Description and numerical tests, *Journal of Climate*, *21* (15), 3642–3659.
- 692 Neale, R. B., et al. (2011), Description of the NCAR Community Atmosphere Model
 693 (CAM5), Tech. rep. NCAR/TN-486+STR, National Center for Atmospheric
 694 Research, Boulder, CO.
- 695 Neale, R. B., J. H. Richter, and M. Jochum (2008), The impact of convection on ENSO:
 696 From a delayed oscillator to a series of events, *Journal of Climate*, *21* (22), 5904–
 697 5924.
- 698 Neelin, J. D., A. Bracco, H. Luo, J. C. McWilliams, and J. E. Meyerson (2010),
 699 Considerations for parameter optimization and sensitivity in climate models,
 700 *Proc. Acad. Nat. Sci.*, *107*, 21,349–21,354, doi: 10.1073/pnas.1015473107.
- 701 Park, S. and C. S. Bretherton (2009), The University of Washington shallow convection
 702 and moist turbulence schemes and their impact on climate simulations with the
 703 Community Atmosphere Model, *Journal of Climate*, *22*, 3449–3469.
- 704 Park, S. (2014), A unified convection scheme, UNICON. Part I: Formulation, *Journal of*
 705 *Atmospheric Sciences*, accepted.
- 706 Pedregosa, F., and CoAuthors (2011), Scikit-learn: Machine learning in Python, *Journal*
 707 *of Machine Learning Research*, *12*, 2825–2830.

- 708 Qian, Y., et al. (2014), Parametric sensitivity analysis of precipitation at global and local
 709 scales in the Community Atmosphere Model CAM5, *J. Adv. Model. Earth Syst.*,
 710 submitted.
- 711 Randall, D. A. (2013), Beyond deadlock. *Geophysical Research Letters*, 40 (22), 5970–
 712 5976.
- 713 Randel, D. L. et al. (1996), A new global water vapor dataset. *Bull. Amer. Meteor. Soc.*,
 714 77, 1233–1246.
- 715 Seo, K.-H., and W. Wang (2010), The Madden-Julian Oscillation simulated in the NCEP
 716 Climate Forecast System Model: The importance of stratiform heating, *Journal of*
 717 *Climate*, 23(18), 4770–4793.
- 718 Song, X. L., G. J. Zhang, and J. L. F. Li (2012), Evaluation of microphysics
 719 parameterization for convective clouds in the NCAR Community Atmosphere
 720 Model CAM5, *Journal of Climate*, 25, 8568-8590, doi:10.1175/jcli-d-11-00563.1.
- 721 Slingo, J. M., et al. (1996), Intraseasonal oscillations in 15 atmospheric general circu-
 722 lation models: Results from and AMIP diagnostic subproject, *Climate Dyn.*, 12,
 723 325–357.
- 724 Sobel, A., and E. Maloney (2013), Moisture modes and the eastward propagation of the
 725 MJO, *Journal of the Atmospheric Sciences*, 70 (1), 187–192, doi:10.1175/JAS-D-
 726 12-0189.1.
- 727 Sperber, K. R. (2003), Propagation and the vertical structure of the Madden-Julian
 728 Oscillation, *Mon. Wea. Rev.*, 131, 3018-3037.
- 729

- 730 Sperber, K. R., S. Gualdi, S. Legutke, and V. Gayler (2005), The Madden-Julian
 731 Oscillation in ECHAM4 Coupled and Uncoupled GCMs, *Climate Dyn.*, *25*, 117-
 732 140.
- 733 Stan, C., M. Khairoutdinov, C. A. DeMott, V. Krishnamurthy, D. M. Straus, D. A.
 734 Randall, J. L. Kinter III, and J. Shukla (2010), An ocean-atmosphere climate
 735 simulation with an embedded cloud resolving model, *Geophys. Res. Lett.*, *37*,
 736 L01702, doi:10.1029/2009GL040822.
- 737 Subramanian, A. C., M. Jochum, A. J. Miller, R. Murtugudde, R. B. Neale, and D. E.
 738 Waliser (2011), The Madden-Julian Oscillation in CCSM4, *Journal of Climate*,
 739 *24*, 6261–6282, doi:10.1175/JCLI-D-11-00031.1.
- 740 Subramanian, A. C., and G. J. Zhang (2014), Diagnosing MJO hindcast biases in NCAR
 741 CAM3 using nudging during the DYNAMO field campaign, *J. Geophys. Res.*
 742 *Atmos.*, *119*, 7231–7253, doi:10.1002/2013JD021370.
- 743 Thayer-Calder, K., and D. A. Randall (2009), The role of convective moistening in the
 744 Madden-Julian oscillation, *J. Atmos. Sci.*, *66*, 3297-3312, doi:
 745 10.1175/2009JAS3081.1
- 746 Tokioka, T., K. Yamazaki, A. Kitoh, and T. Ose (1988), The equatorial 30-60 day
 747 oscillation and the Arakawa-Schubert penetrative cumulus parameterization, *J.*
 748 *Meteor. Soc. Japan*, *66*, 883–901.
- 749 Waliser, D. E., K. M. Lau, and J. H. Kim (1999), The influence of coupled sea surface
 750 temperatures on the Madden–Julian oscillation: A model perturbation experiment,
 751 *J. Atmos. Sci.*, *56*, 333–358.

- 752 Wheeler, M. C. and H. H. Hendon, 2004: An all-season real-time multivariate MJO
 753 index: Development of an index for monitoring and prediction. *Mon. Wea. Rev.*,
 754 **132**, 1917–1932.
- 755 Wheeler, M., and G. N. Kiladis (1999), Convectively coupled equatorial waves: Analysis
 756 of clouds and temperature in the wavenumber–frequency domain, *Journal of the*
 757 *Atmospheric Sciences*, **56**(3), 374–399, doi:10.1175/1520-
 758 0469(1999)056<0374:CCEWAO>2.0.CO;2.
- 759 Woolnough, S. J., F. Vitart, and M. A. Balmaseda (2007), The role of the ocean in the
 760 madden– julian oscillation: Implications for mjo prediction, *Quarterly Journal of*
 761 *the Royal Meteorological Society*, **133**(622), 117–128, doi:10.1002/qj.4.
- 762 Yang, B., et al. (2013), Uncertainty quantification and parameter tuning in the CAM5
 763 Zhang- McFarlane convection scheme and impact of improved convection on the
 764 global circulation and climate, *Journal of Geophysical Research: Atmospheres*,
 765 doi:10.1029/2012JD018213.
- 766 Zhang, C. (2005), Madden-Julian Oscillation, *Rev. Geophys.*, **43** (2),
 767 doi:10.1029/2004RG000158.
- 768 Zhang, C., J. Ling, S. M. Hagos, W.-K. Tao, S. Lang, Y. N. Takayabu, S. Shige, M.
 769 Katsumata, W. S. Olson, and T. L’Ecuyer (2010), MJO Signals in Latent Heating:
 770 Results from TRMM Retrievals, *J. Atmos. Sci* , **67**, 3488–3508.
- 771 Zhang, C., J. Gottschalck, E. D. Maloney, M. W. Moncrieff, F. Vitart, D. E. Waliser, B.
 772 Wang, and M. C. Wheeler (2013), Cracking the MJO nut, *Geophys. Res. Lett.*, **40**,
 773 1223–1230, doi:10.1002/grl.50244.

- 774 Zhang, G. J., and N. A. McFarlane (1995), Sensitivity of climate simulations to the
775 parameterization of cumulus convection in the Canadian Climate Centre general
776 circulation model. *Atmos.-Ocean*, 33, 407-446.
- 777 Zhang, G. J., and M. Mu (2005), Simulation of the Madden–Julian Oscillation in the
778 NCAR CCM3 using a revised Zhang–McFarlane convection parameterization
779 scheme, *Journal of Climate*, 18(19), 4046–4064, doi:10.1175/JCLI3508.1.
- 780 Zhou, L., R. B. Neale, M. Jochum, and R. Murtugudde (2012), Improved Madden–Julian
781 Oscillations with improved physics: The impact of modified convection
782 parameterizations, *Journal of Climate*, 25(4), 1116–1136,
783 doi:10.1175/2011JCLI4059.1.
784

List of Figures

FIGURE 1. Lag-longitude correlation coefficients of TRMM precipitation averaged from 10°S - 10°N with TRMM precipitation averaged over the (a) the Indian Ocean region (70°E - 90°E, 5°S - 5°N and (b) for the West Pacific Ocean region (130°E - 150°E, 5°S - 5°N). The TRMM data are band-pass filtered for 20 – 90 days. The correlations are computed using data from the November to April half of the year.

FIGURE 2. TRMM November to April wavenumber-frequency spectra of 10°N - 10°S averaged precipitation. The abscissa is for frequency in units of cycles per day with positive values indicating eastward propagating waves. The ordinate is for zonal wavenumber. Solid boxes indicate regions for averaging east and west power and correspond to periods between 20 and 90 days and for wavenumbers 1 – 5. Individual November to April spectra were calculated for each year, and then averaged over all years of data. Only the climatological seasonal cycle and time mean were removed before calculating spectra.

FIGURE 3. Joint histogram across the ensemble of East-West Power Ratio (*wePwrRatio*) and lead-lag/longitude pattern correlation (*patCorACIO*) using (a) GPCP and (b) TRMM precipitation observations. The number of models within a given region are indicated by the color shading whose legend is shown to the right of the plot. The star indicates the values of these metrics for the CAM5 with its default settings. The large black circle at the top of the plots indicates the value calculated from observations and if matched by a model would represent a perfect simulation.

FIGURE 4. Parameter importance feature scores estimated by the random forest technique for *patCorACIO*, *patCorACWP*, and *wePwrRatio*. The score indicates the

relative importance of a given physical parameter to the variations in the values the MJO metrics of *patCorACIO*, *patCorACWP*, and *wePwrRatio*.

FIGURE 5. Marginal distributions of parameter likelihood values on the ordinate for five deep convection parameters using random forest evaluations and observations of *patCorACIO*, *patCorACWP* and *wePwrRatio*. The abscissa displays the scaled parameter values between 0 (minimum) and 1 (maximum), and the vertical red lines denote the default parameter values used in CAM5. These plots can be used to indicate the relative likelihood of a given parameter value. For example, CAM5 simulations in which *zmconv_c0_ocn* is set to its minimum value are much more likely than any other value including CAM5's default to lead to simulations which more closely match the observed values of *patCorACIO*, *patCorACWP* and *wePwrRatio*.

FIGURE 6. As in FIGURE 1a, except with the addition of the lag-longitude correlation coefficients of 850 hPa zonal wind anomalies (contour lines) in addition to that for the intra-seasonal precipitation anomalies (color shading). Results are shown for the (a) observations and the (b) *Default*, (c) *UQ-Rec*, and (d) *PPE-Best* simulations. Observations are from TRMM for precipitation and ERA-Interim for 850 hPa zonal wind.

FIGURE 7. As in FIGURE 2, but for the (a) *Default*, (b) *UQ-Rec* and (c) *PPE-Best* simulations. Note that the color scale of the *Default* simulation covers only $\frac{1}{2}$ the range of the *UQ-Rec* and *PPE-Best* simulations.

FIGURE 8. Leading multivariate combined EOF of the band-passed OLR, 850-hPa and 200 hPa zonal wind averaged from 15°S to 15°N for November to April for the (a)

observations and the (b) *Default*, (c) *UQ-Rec* and (d) *PPE-Best* simulations. Observations are from ERA-Interim for winds and *Liebmann and Smith* [1996] for OLR.

FIGURE 9. Power-spectral density plots of the leading CEOF (FIGURE 8) projected onto the unfiltered data with only the seasonal cycle removed for the (a) observations and the (b) *Default*, (c) *UQ-Rec*, and (d) *PPE-Best* simulations. The 90% and 95% confidence limits on a red noise spectra are plotted for comparison.

FIGURE 10. Composite November to April band-pass filtered OLR as a function of the 8 phases of the MJO with time progressing downwards. The composite is based on $PC1^2 + PC2^2 > 1$ for (a) the observations and the (b) *Default*, (c) *UQ-Rec*, (d) *PPE-Best* simulations. The units on OLR are in $W\ m^{-2}$.

FIGURE 11. As in FIGURE 10 but for 850 hPa zonal wind. The units on the zonal wind are in $m\ sec^{-1}$.

FIGURE 12. Longitude-pressure cross-sections of $15^{\circ}S$ to $15^{\circ}N$ averaged specific humidity anomalies linearly regressed onto $10^{\circ}N - 10^{\circ}S$ averaged 20 – 90 day band-passed precipitation at $120^{\circ}E$ for (a) ERA-Interim and the (b) *Default*, (c) *UQ-Rec*, and (d) *PPE-Best* simulations. Positive values are indicated by solid contours whereas negative values are indicated by dashed contours. Shading indicates where anomalies are significant at the 95% level.

FIGURE 13. As in FIGURE 12, but for diabatic heating.

FIGURE 14. Longitude-pressure cross-sections of water vapor specific humidity differences in $g\ kg^{-1}$ between the ERA-Interim re-analysis and the (a) *Default*, (b) *UQ-Rec*, (c) *PPE-Best*, and (d) *OAT38* simulations. Differences are averaged over the months

852 of November through April and from 15°N-15°S with positive values indicating that the
853 simulated specific humidity is larger than that in the re-analysis.

854 TABLE 1. Summary of CAM5 parameterizations.

Parameterizations	CAM5 Implementation
Radiation	Rapid Radiative Transfer Model - Global [<i>Iacono et al., 2008</i>]
Shallow convection	Mass flux scheme with convective inhibition closure [<i>Park and Bretherton, 2009</i>]
Deep convection	Bulk mass flux with CAPE closure and an entraining plume [<i>Zhang and McFarlane, 1995; Neale et al., 2008</i>]
Planetary boundary layer and turbulence	Moist turbulence scheme based on diagnostic turbulent kinetic energy [<i>Bretherton and Park, 2009</i>]
Cloud microphysics and macrophysics	Prognostic double moment microphysics, [<i>Morrison and Gettelman, 2008; Gettelman et al., 2010</i>] and diagnostic cloud fraction scheme
Aerosols	Modal aerosol model [<i>Liu et al., 2012</i>]

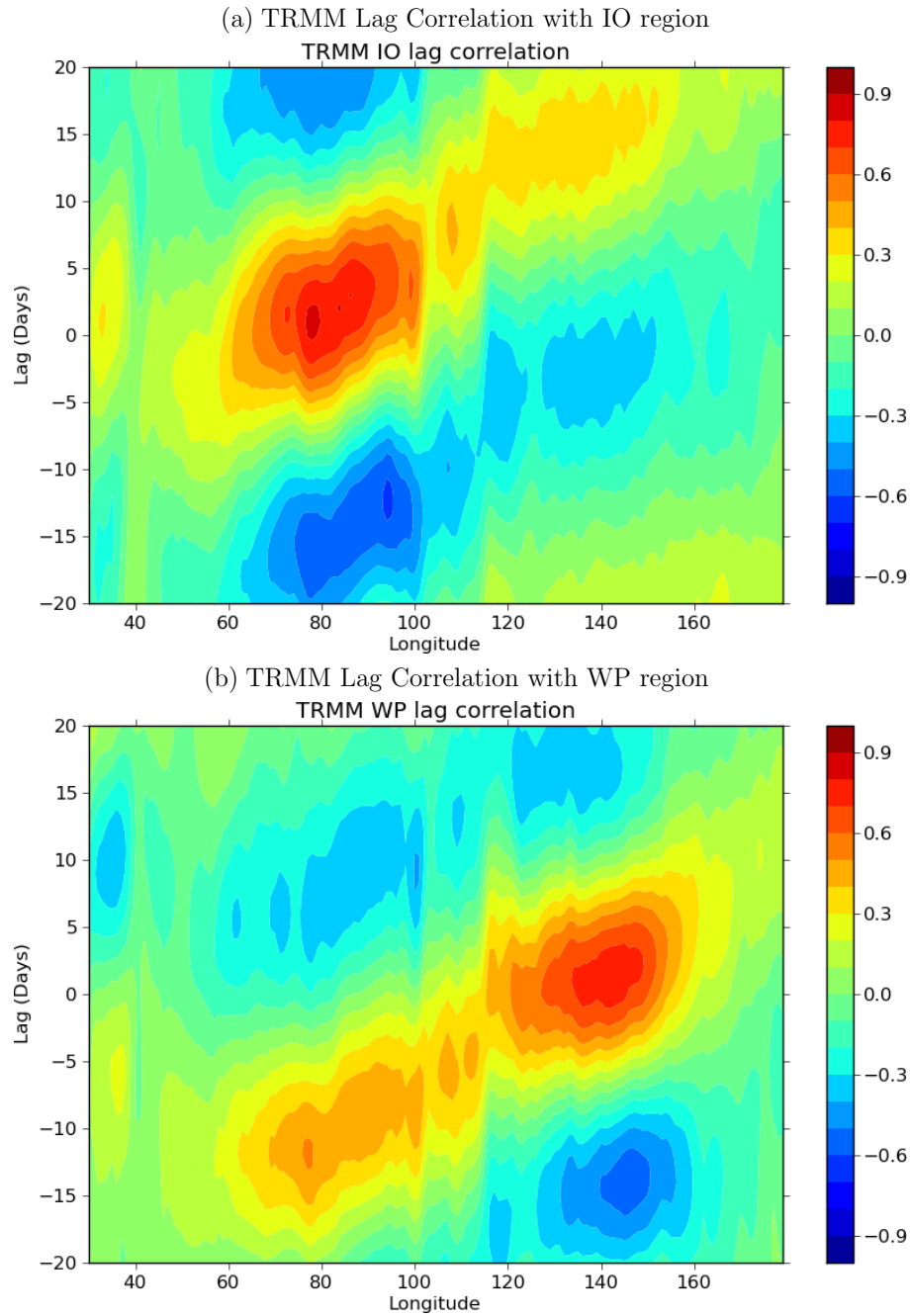
1 TABLE 2. Parameters varied in the perturbed parameter ensemble.
 2

Model Variable	Variable Description	Parameterization	Minimum Value	Default Value	Maximum Value
dust_emis_fact	Dust emission tuning factor	Aerosol	0.21	0.35	0.86
cldfrc_rhminh	Threshold relative humidity for high-level clouds	Large-scale cloud	0.65	0.8	0.85
cldfrc_rhminl	Threshold relative humidity for low-level clouds	Large-scale cloud	0.8	0.8875	0.99
cldwatmi_ai	Fall speed parameter for stratiform cloud ice	Large-scale cloud	350	700	1400
cldwatmi_as	Fall speed parameter for stratiform snow	Large-scale cloud	5.86	11.72	23.44
cldwatmi_cdn1	Cloud droplet number limiter	Large-scale cloud	0	0	1×10^{-6}
cldwatmi_dcs	Autoconversion size threshold for ice to snow	Large-scale cloud	0.0001	0.0004	0.0005
cldwatmi_eii	Collection efficiency for the aggregation of ice	Large-scale cloud	0.001	0.1	1
cldwatmi_qcvar	Inverse relative variance of sub-grid scale cloud water	Large-scale cloud	0.5	2	5
eddydiff_a2l	Moist entrainment enhancement parameter	Turbulence	10	30	50
micropa_wsubimax	Maximum sub-grid scale vertical velocity for ice nucleation	Large-scale cloud	0.1	0.2	1
micropa_wsubmin	Minimum sub-grid scale vertical velocity for liquid nucleation	Large-scale cloud	0	0.2	1
uwschcu_criqc	Maximum updraft condensate in shallow convection	Shallow convection	0.0005	0.007	0.0015
uwschcu_keyvp	Evaporative efficiency of shallow convection precipitation	Shallow convection	1×10^{-6}	2×10^{-6}	2×10^{-5}
uwschcu_rkm	Scaling factor for shallow convection entrainment rate	Shallow convection	8	14	16
uwschcu_rpen	Penetrative efficiency of shallow convection updraft	Shallow convection	1	5	10
zmconv_alfa	Initial deep convection cloud downdraft mass flux	Deep convection	0.05	0.1	0.6
zmconv_c0_lnd	Deep convection autoconversion coefficient over land	Deep convection	0.001	0.0059	0.01
zmconv_c0_ocn	Deep convection autoconversion coefficient over ocean	Deep convection	0.001	0.045	0.1
zmconv_dmpdz	Fractional mass entrainment rate for deep convection	Deep convection	0.0002	0.001	0.002
zmconv_ke	Evaporation efficiency of deep convection precipitation	Deep convection	5×10^{-7}	1×10^{-6}	1×10^{-5}
zmconv_tau	Convective adjustment time scale for deep convection	Deep convection	1800	3600	28800

1 TABLE 3. Bias and root-mean-square (RMS) errors calculated over a global domain for
 2 climatological December-January-February averages between observations and various
 3 model configurations. Model simulations are compared to observations of GPCP
 4 precipitation, CERES EBAF shortwave cloud radiative effect (SWCRE), ocean-only
 5 NVAP liquid water path (LWP), and CERES EBAF OLR.

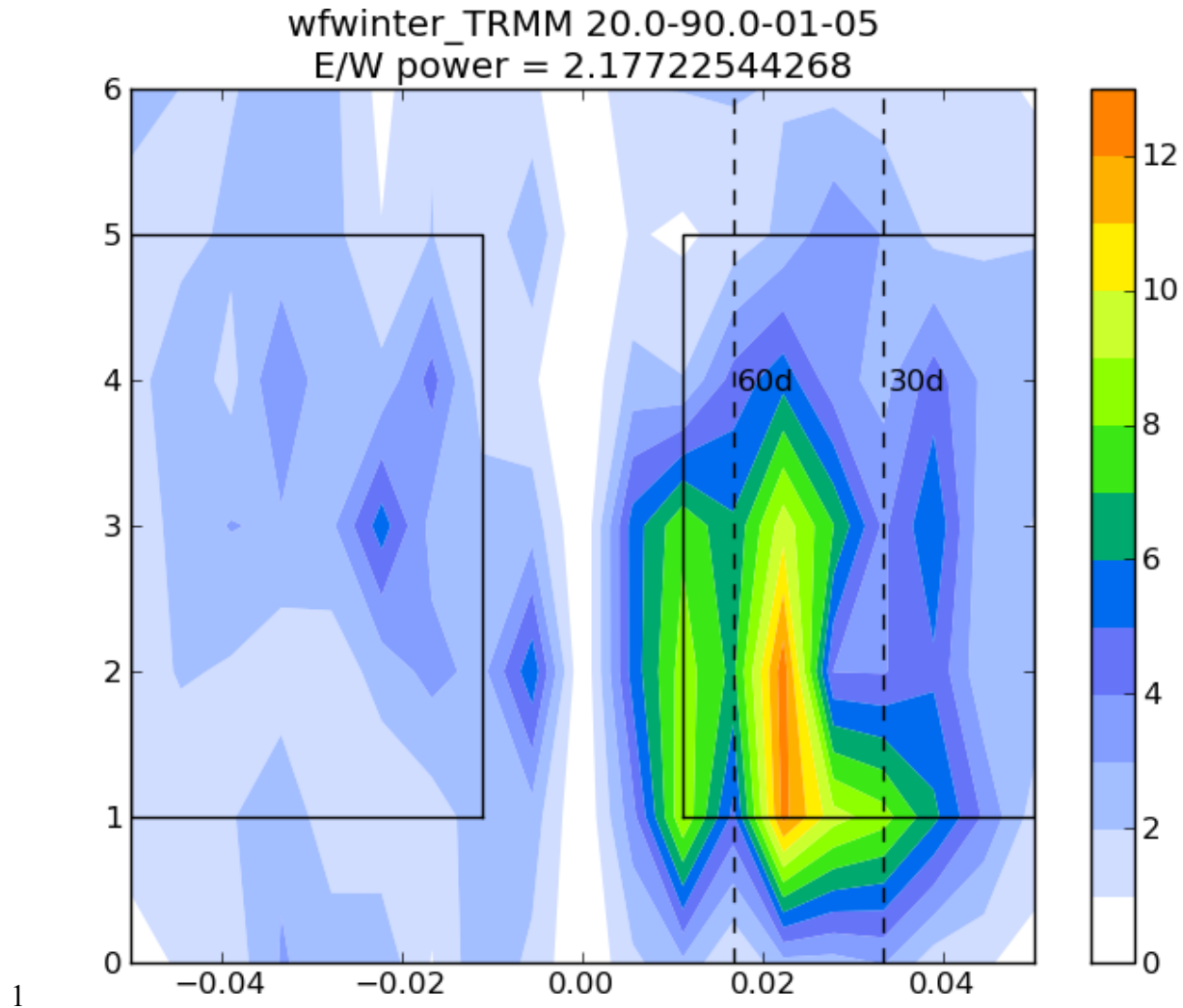
Model	GPCP (mm d^{-1})		CERES EBAF SWCRE (W m^{-2})		NVAP LWP (g m^{-2})		CERES EBAF OLR (W m^{-2})	
	Bias	RMS	Bias	RMS	Bias	RMS	Bias	RMS
<i>Default</i>	0.301	1.284	-2.76	21.25	-35.32	39.71	-3.95	9.967
<i>UQ-Rec</i>	0.179	1.314	-20.82	36.17	216.54	355.20	-7.46	13.12
<i>PPE-Best</i>	0.252	1.501	-27.655	41.089	188.29	303.08	-7.99	13.90
<i>OAT38</i>	0.225	1.232	-18.629	34.881	181.95	314.64	-7.59	13.32

6

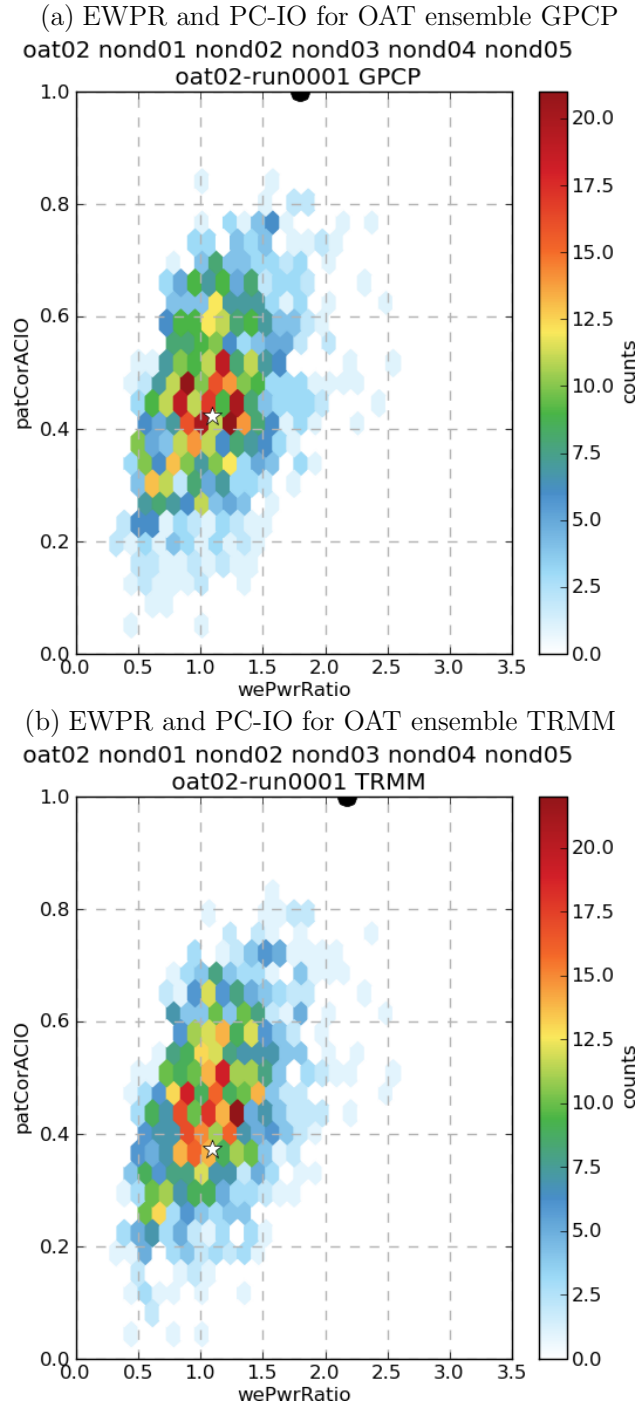


1

2 FIGURE 1. Lag-longitude correlation coefficients of TRMM precipitation averaged from
 3 10°S - 10°N with TRMM precipitation averaged over the (a) the Indian Ocean region
 4 (70°E - 90°E, 5°S - 5°N and (b) for the West Pacific Ocean region (130°E - 150°E, 5°S -
 5 5°N). The TRMM data are band pass filtered for 20 – 90 days. The correlations are
 6 computed using data from the November to April half of the year.

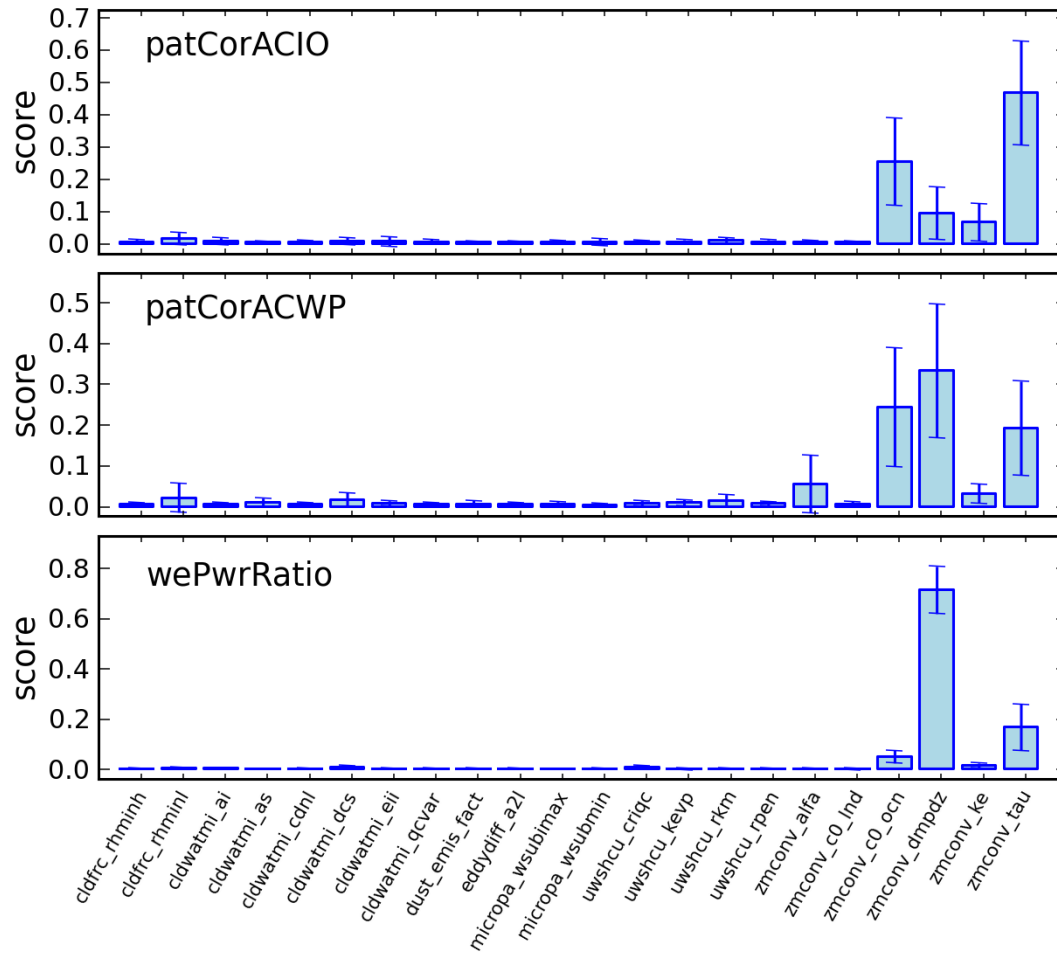


2 FIGURE 2. TRMM November to April wavenumber-frequency spectra of 10°N - 10°S
 3 averaged precipitation. The abscissa is for frequency in units of cycles per day with
 4 positive values indicating eastward propagating waves. The ordinate is for zonal
 5 wavenumber. Solid boxes indicate regions for averaging east and west power and
 6 correspond to periods between 20 and 90 days and for wavenumbers 1 – 5. Individual
 7 November to April spectra were calculated for each year, and then averaged over all
 8 years of data. Only the climatological seasonal cycle and time mean were removed before
 9 calculating spectra.



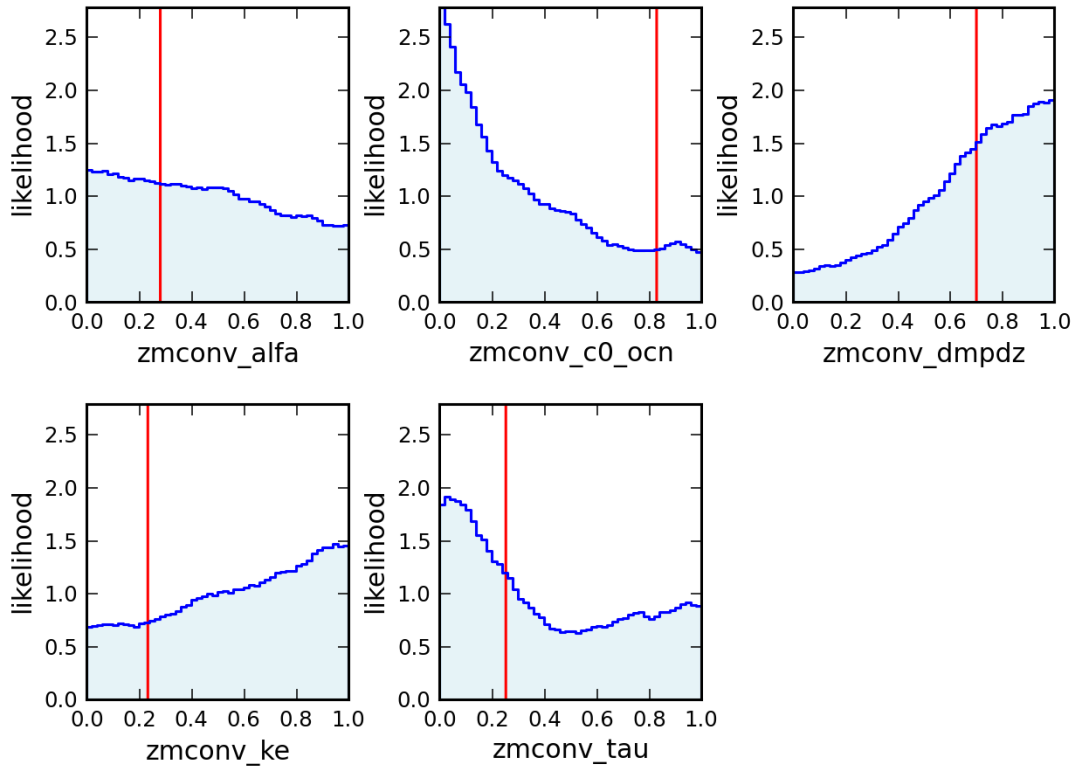
1

2 FIGURE 3. Joint histogram across the ensemble of East-West Power Ratio ($wePwrRatio$)
 3 and lead-lag/longitude pattern correlation ($patCorACIO$) using (a) GPCP and (b) TRMM
 4 precipitation observations. The number of models within a given region are indicated by
 5 the color shading whose legend is shown to the right of the plot. The star indicates the
 6 values of these metrics for the CAM5 with its default settings. The large black circle at
 7 the top of the plots indicates the value calculated from observations and if matched by a
 8 model would represent a perfect simulation.



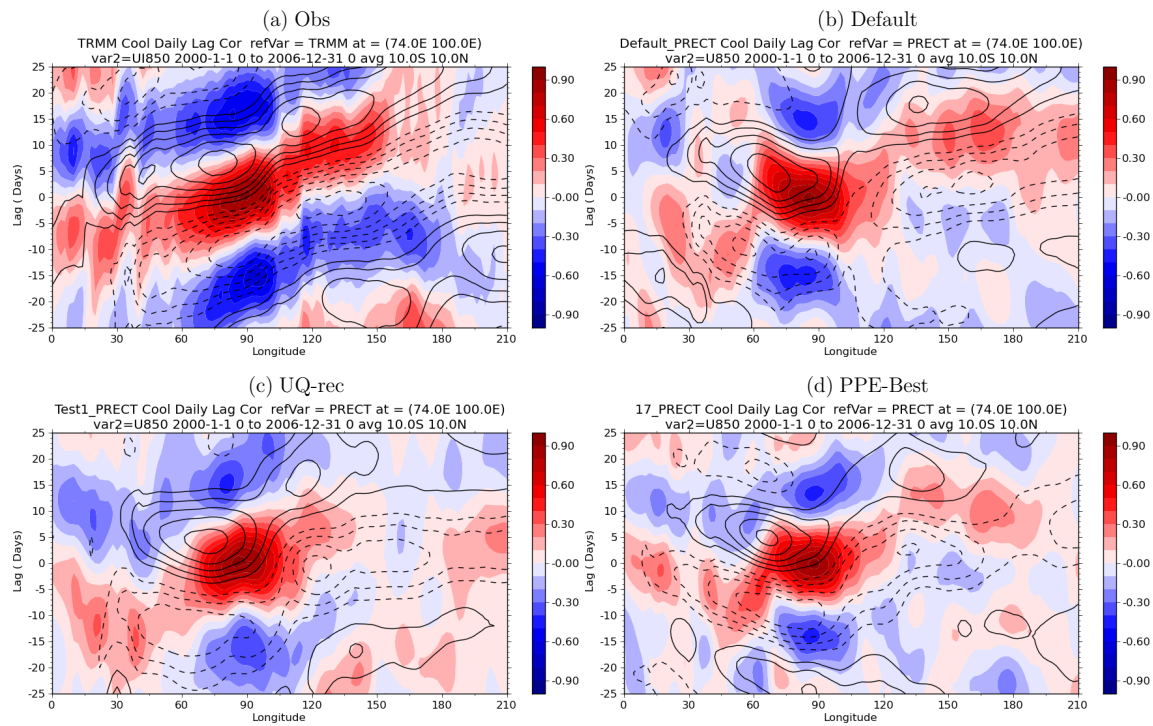
1

2 FIGURE 4. Parameter importance feature scores estimated by the random forest
3 technique for *patCorACIO*, *patCorACWP*, and *wePwrRatio*. The score indicates the
4 relative importance of a given physical parameter to the variations in the values the MJO
5 metrics of *patCorACIO*, *patCorACWP*, and *wePwrRatio*.



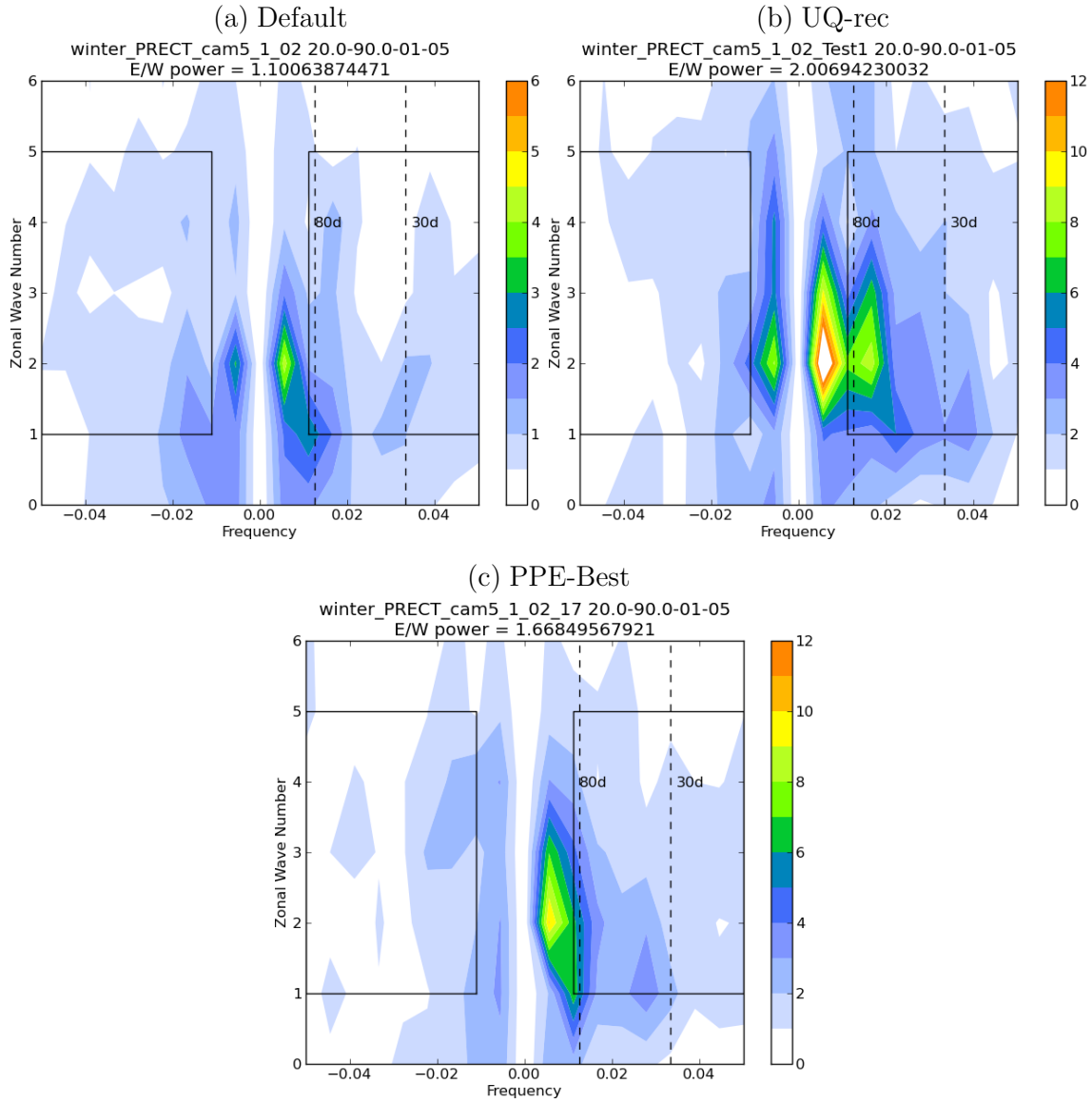
1

2 FIGURE 5. Marginal distributions of parameter likelihood values on the ordinate for 5
3 deep convection parameters using random forest evaluations and observations of
4 *patCorACIO*, *patCorACWP* and *wePwrRatio*. The abscissa displays the scaled parameter
5 values between 0 (minimum) and 1 (maximum), and the vertical red lines denote the
6 default parameter values used in CAM5. These plots can be used to indicate the relative
7 likelihood of a given parameter value. For example, CAM5 simulations in which
8 *zmconv_c0_ocn* is set to its minimum value are much more likely than any other value
9 including CAM5's default to lead to simulations which more closely match the observed
10 values of *patCorACIO*, *patCorACWP* and *wePwrRatio*.



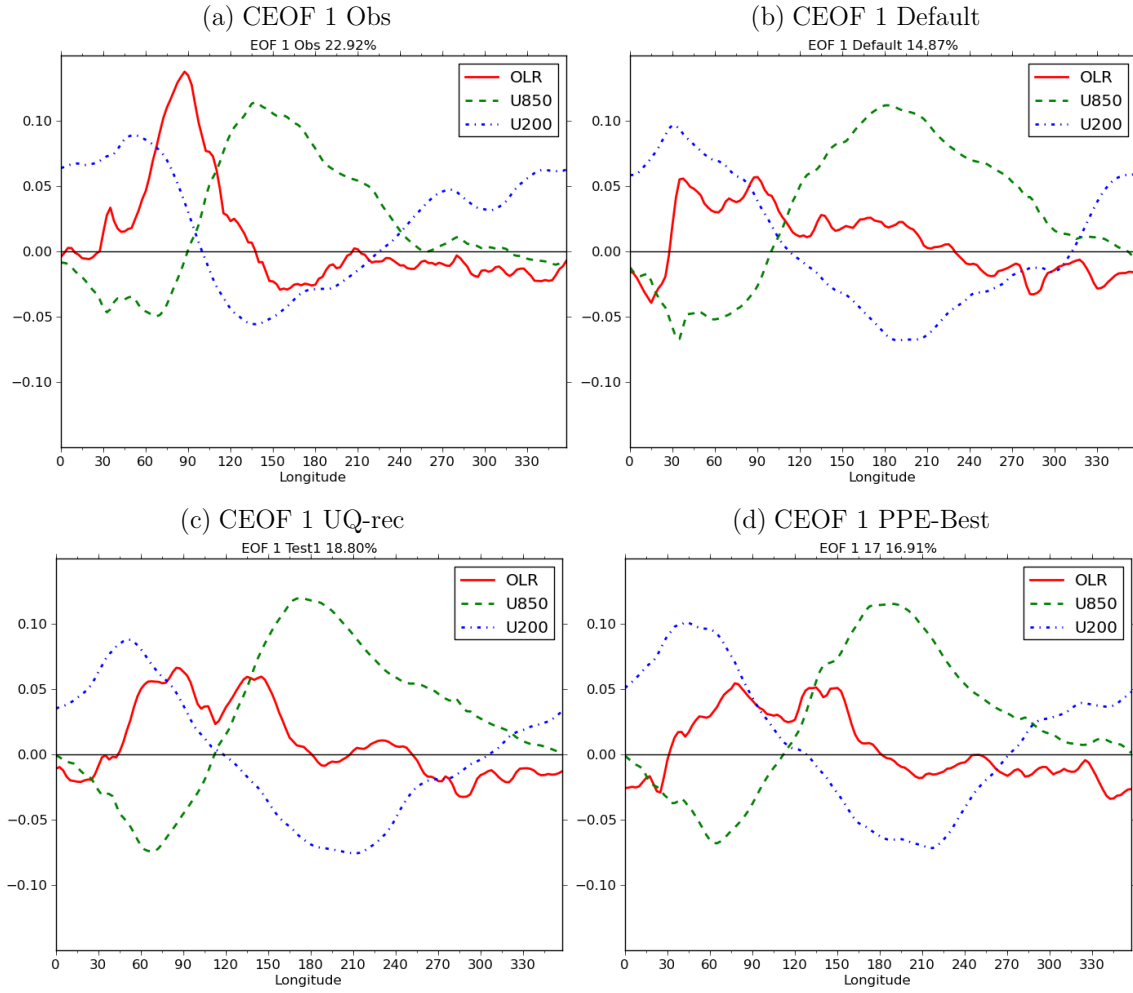
1

2 FIGURE 6. As in FIGURE 1a, except with the addition of the lag-longitude correlation
 3 coefficients of 850 hPa zonal wind anomalies (contour lines) in addition to that for the
 4 intra-seasonal precipitation anomalies (color shading). Results are shown for the (a)
 5 observations and the (b) *Default*, (c) *UQ-Rec*, and (d) *PPE-Best* simulations.
 6 Observations are from TRMM for precipitation and ERA-Interim for 850 hPa zonal
 7 wind.



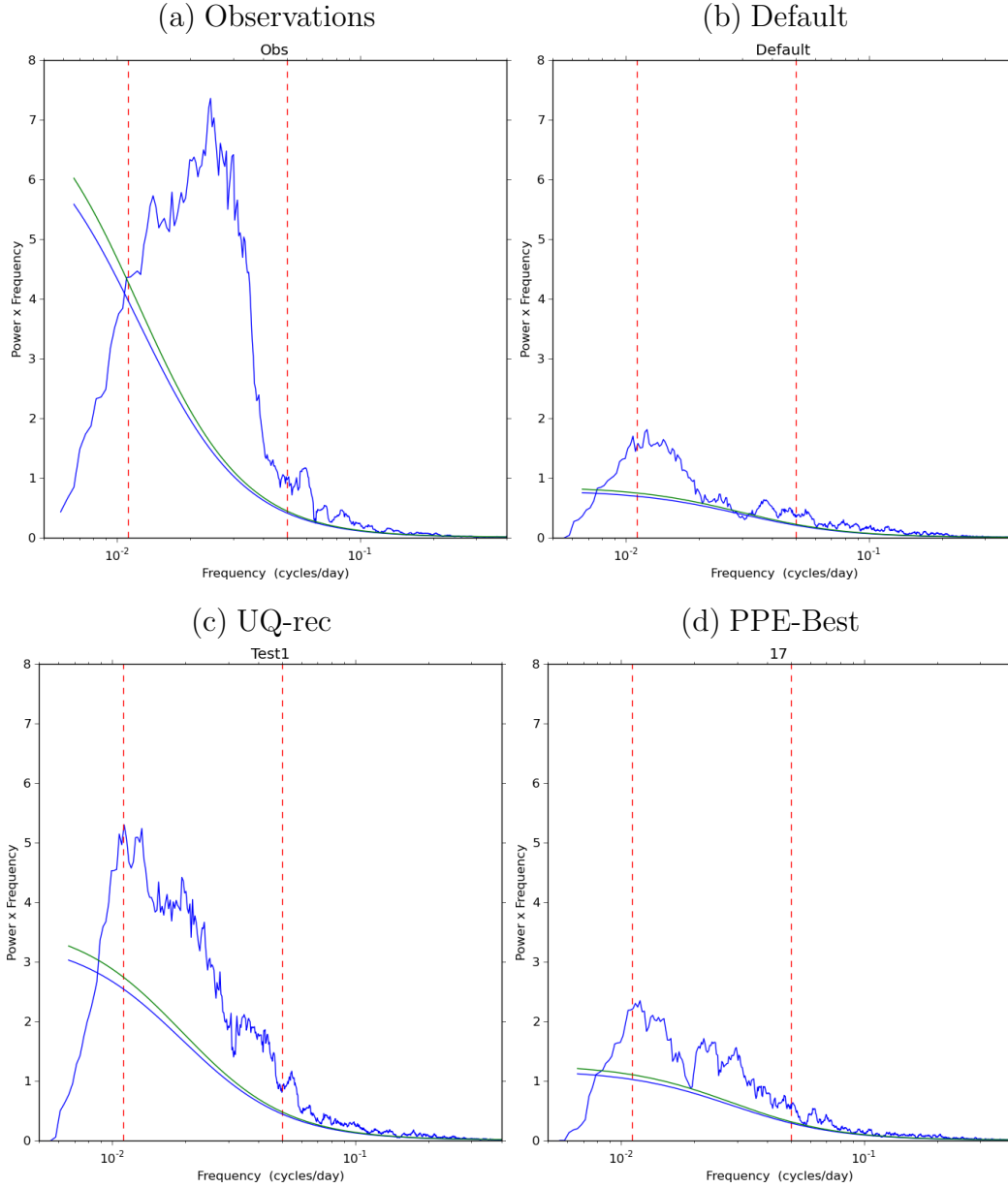
1

2 FIGURE 7. As in FIGURE 2, but for the (a) *Default*, (b) *UQ-Rec* and (c) *PPE-Best*
 3 simulations. Note that the color scale of the *Default* simulation covers only $\frac{1}{2}$ the range
 4 of the *UQ-Rec* and *PPE-Best* simulations.



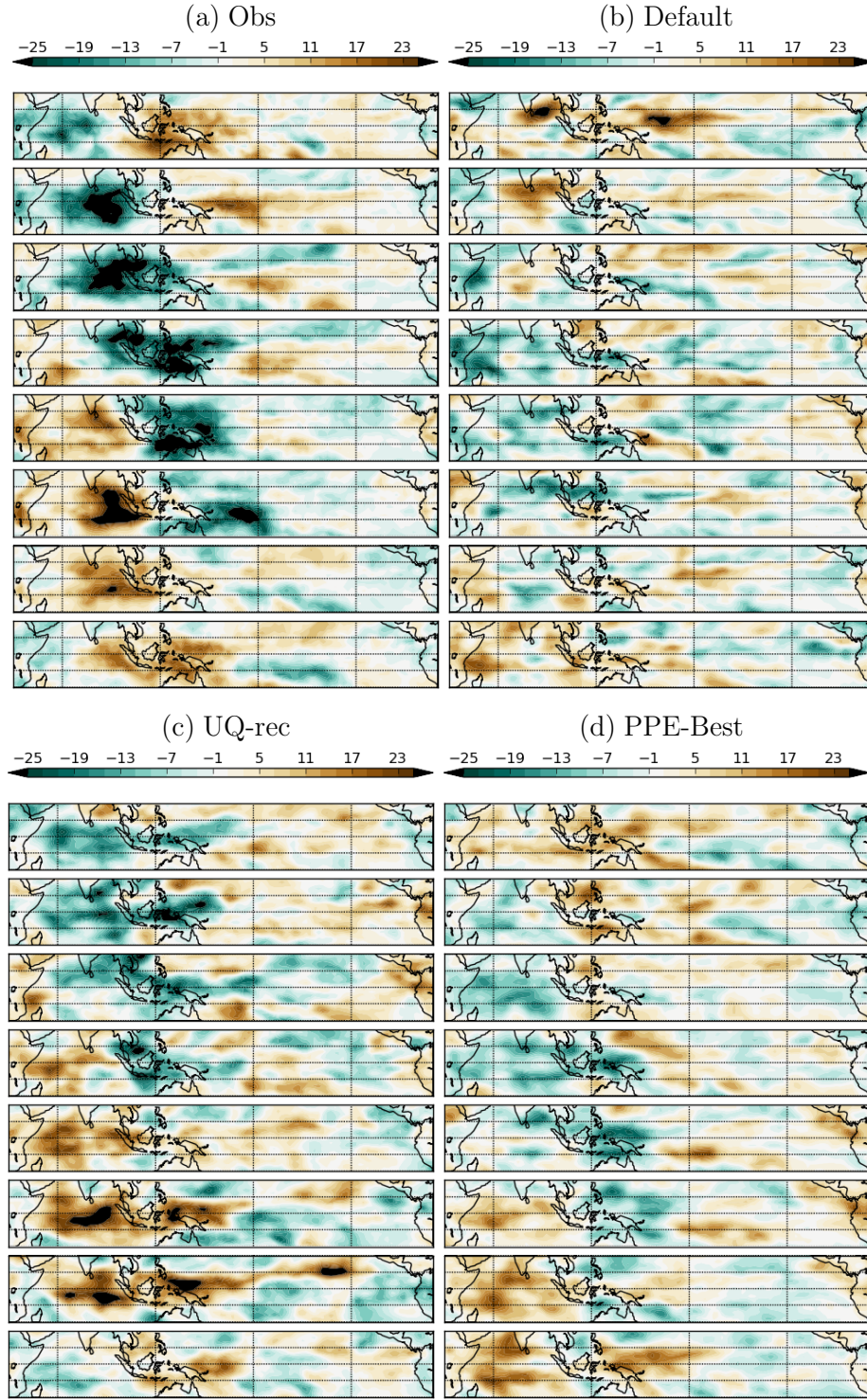
1

2 FIGURE 8. Leading multivariate combined EOF of the band passed OLR, 850-hPa and
3 200 hPa zonal wind averaged from 15°S to 15°N for November to April for the (a)
4 observations and the (b) *Default*, (c) *UQ-Rec* and (d) *PPE-Best* simulations. Observations
5 are from ERA-Interim for winds and *Liebmann and Smith* [1996] for OLR.



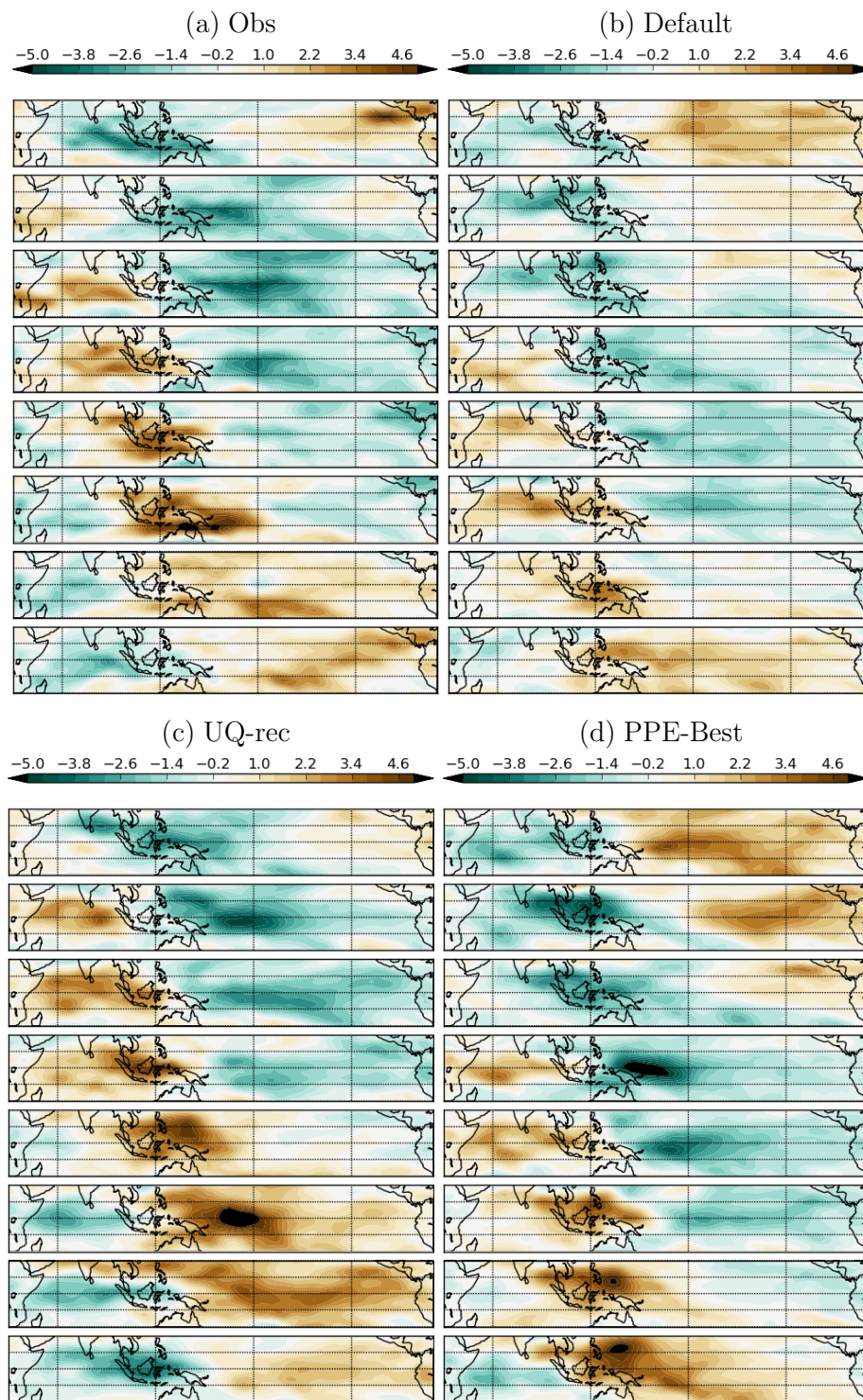
1

2 FIGURE 9. Power-spectral density plots of the leading CEOF (FIGURE 8) projected
 3 onto the unfiltered data with only the seasonal cycle removed for the (a) observations and
 4 the (b) *Default*, (c) *UQ-Rec*, and (d) *PPE-Best* simulations. The 90% and 95% confidence
 5 limits on a red noise spectra are plotted for comparison.



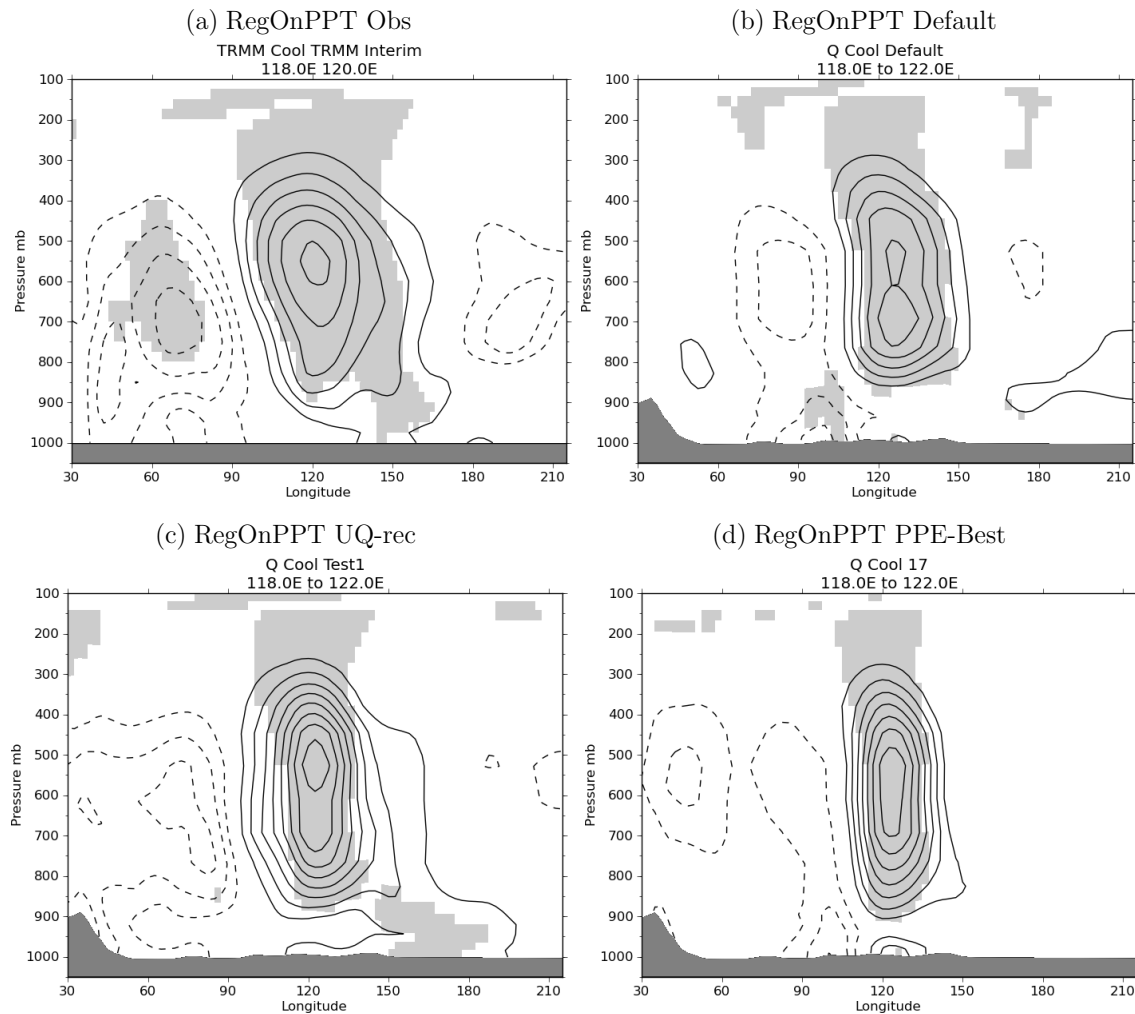
1

2 FIGURE 10. Composite November to April band pass filtered OLR as a function of the 8
3 phases of the MJO with time progressing downwards. The composite is based on $PC1^2 +$
4 $PC2^2 > 1$ for (a) the observations and the (b) *Default*, (c) *UQ-Rec*, (d) *PPE-Best*
5 simulations. The units on OLR are in $W m^{-2}$.



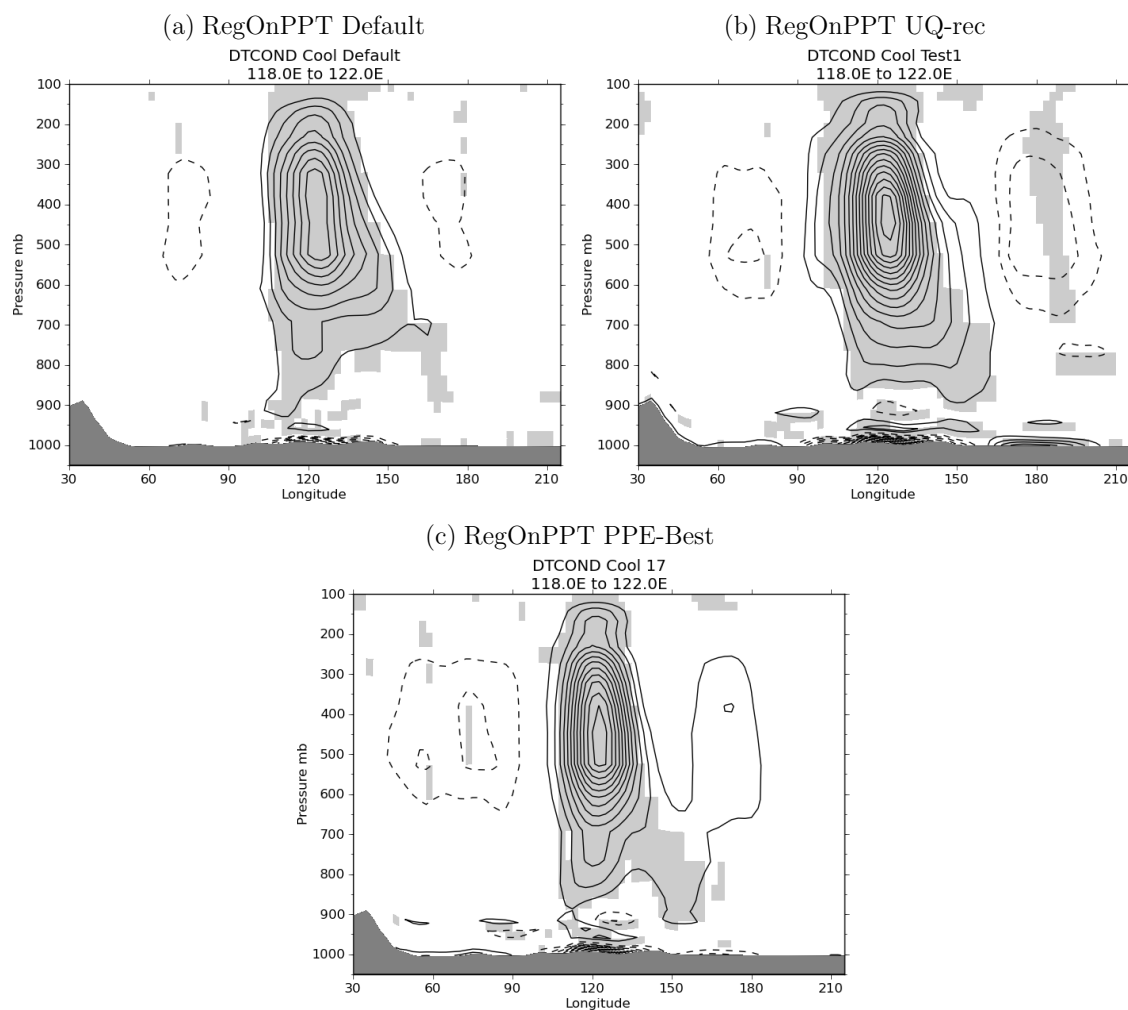
1

2 FIGURE 11. As in FIGURE 10 but for 850 hPa zonal wind. The units on the zonal wind
 3 are in m sec^{-1} .



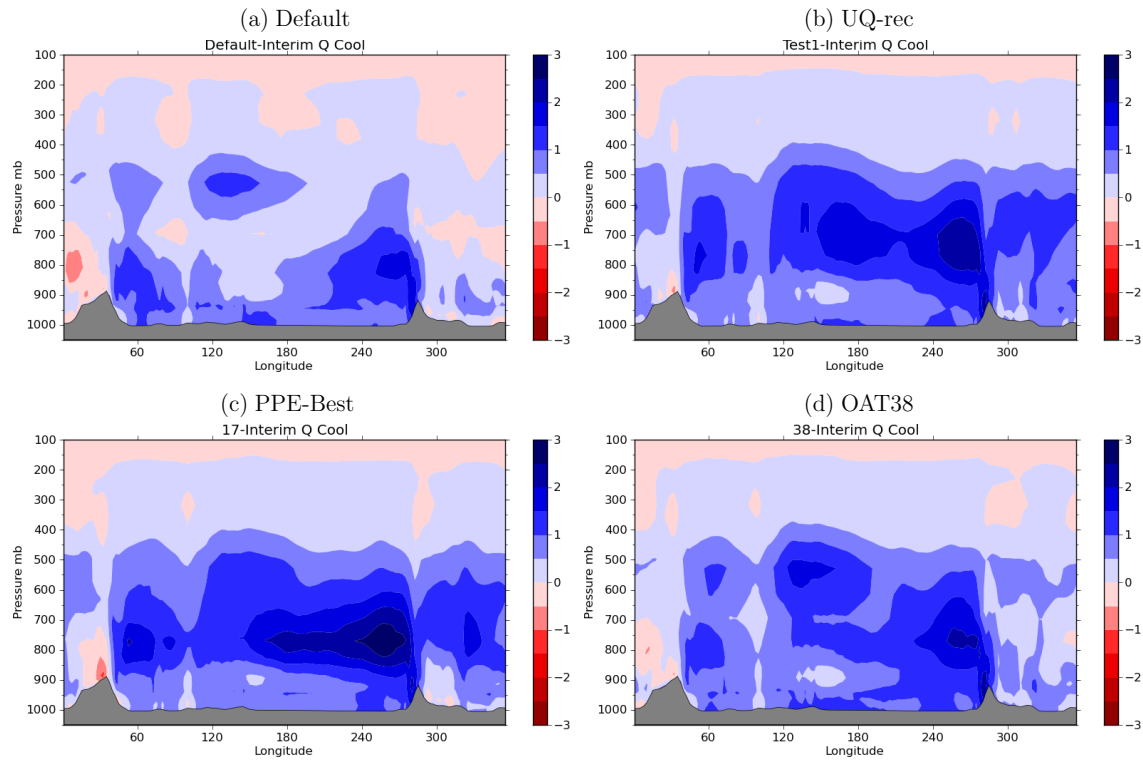
1

2 FIGURE 12. Longitude-pressure cross-sections of 15°S to 15°N averaged specific
3 humidity anomalies linearly regressed onto 10°N - 10°S averaged 20 – 90 day band-
4 passed precipitation at 120°E for (a) ERA-Interim and the (b) *Default*, (c) *UQ-Rec*, and
5 (d) *PPE-Best* simulations. Positive values are indicated by solid contours whereas
6 negative values are indicated by dashed contours. Shading indicates where anomalies are
7 significant at the 95% level.



1

2 FIGURE 13. As in FIGURE 12 but for diabatic heating.



1

2 FIGURE 14. Longitude-pressure cross-sections of water vapor specific humidity
 3 differences in g kg^{-1} between the ERA-Interim re-analysis and the (a) *Default*, (b) *UQ-*
 4 *Rec*, (c) *PPE-Best*, and (d) *OAT38* simulations. Differences are averaged over the months
 5 of November through April and from 15°N - 15°S with positive values indicating that the
 6 simulated specific humidity is larger than that in the re-analysis.

7

8

